ChemComm

HIGHLIGHT

View Article Online
View Journal | View Issue

Cite this: *Chem. Commun.*, 2025, **61**, 4739

Bifunctional transition-metal catalysts for energy-saving hydrogen generation from nitrogenous wastewater

Yue Zhou,[a] Liang Zhang,[a] Xin Yang,*[a] Guiyue Xu,[a] Chao Meng,*[bc] Guoqiang Li,[a] Yan Lin,[a] Chongzheng Sun,[a] Ning Zhang,[a] Ran Yi,*[d] Kun Zhang[b] and Lichao Jia *[e]

Wastewater from industrial chemical synthesis, agricultural activities, and domestic sewage usually contains high levels of nitrogenous compounds, endangering environmental health and human well-being. Nitrogenous wastewater electrolysis (NWE), despite its ecological merits, is inherently hampered by sluggish kinetics. To improve process efficiency, lower costs, and avoid cross-contamination between the anode and cathode, a range of bifunctional transition-metal catalysts capable of efficient operation at both electrodes have recently been developed. This review outlines the progress in these catalysts for the energy-saving production of hydrogen from nitrogenous wastewater, including urea, hydrazine, and ammonia. It highlights their dual role in both degrading nitrogenous pollutants and generating hydrogen energy. The review meticulously introduces the key performance metrics of the NWE system and surveys the latest advancements in bifunctional transition-metal catalysts, along with their catalytic mechanisms. It culminates in a detailed summary and comparative analysis of representative bifunctional catalysts, emphasizing their electricity consumption and energy-saving efficiency. Lastly, the existing challenges and research prospects are thoroughly discussed.

Received 13th January 2025,
Accepted 28th February 2025

DOI: 10.1039/d5cc00206k

rsc.li/chemcomm

1. Introduction

Environmental degradation and the looming energy crisis have catalyzed a concerted push towards the development of sustainable and eco-friendly energy alternatives to conventional fossil fuels.[1–3] Molecular hydrogen (H_2), renowned for its high energy density and environmental benignity, stands out as an ideal energy carrier.[4–6] Currently, the main techniques for hydrogen generation are steam reforming of natural gas and other fossil fuels, which accounts for approximately 95% of global H_2 output. These approaches always require high temperature and invariably result in carbon emissions.[7] Among the numerous ways for producing H_2, electrocatalytic water splitting is recognized a potential energy conversion technique because of its low-cost and zero-carbon emission.[8–12] This process bifurcates into two electrochemical reactions: the hydrogen evolution reaction (HER) at the cathode and the oxygen evolution reaction (OER) at the anode, culminating in a theoretical voltage of 1.23 V to initiate overall water splitting (OWS).[13–15] Nonetheless, the sluggish kinetics of the OER's four-electron transfer mechanism pose a significant barrier, often requiring voltages exceeding 1.8 V for effective H_2 generation, thereby substantially increasing extra energy consumption.[16]

To overcome the aforementioned challenges, hybrid water electrolysis (HWE) systems have emerged as a promising strategy for hydrogen generation.[17,18] These innovative systems ingeniously integrate the oxidation of small molecules within the electrolyte with the HER, leveraging thermodynamically advantageous processes to reduce the energy expenditure associated with water splitting, as illustrated in Fig. 1. Water from industrial chemical synthesis, agricultural production, and domestic sewage, in particular, contains a high concentration of nitrogenous chemicals including urea, hydrazine, and ammonia, causing environmental pollution and human health concerns.[19–21] Compared to the OER, the selected nitrogenous molecules oxidation reaction (NmOR) operates at lower

[a] *College of Energy Storage Technology, Shandong University of Science and Technology, Qingdao 266590, China. E-mail: yangx@sdust.edu.cn*
[b] *College of Electrical Engineering and Automation, Shandong University of Science and Technology, Qingdao 266590, China. E-mail: ChaoMeng@sdust.edu.cn*
[c] *State Key Laboratory of Heavy Oil Processing, Institute of New Energy, China University of Petroleum (East China), Qingdao 266580, China*
[d] *Department of Civil and Environmental Engineering, University of Wisconsin-Madison, Madison 53706, USA. E-mail: ryi22@wisc.edu*
[e] *School of Materials Science and Engineering, State Key Laboratory of Materials Processing and Die & Mould Technology, Huazhong University of Science and Technology, Wuhan 430074, China. E-mail: jialc@hust.edu.cn*

potentials, not only significantly reducing the energy input required for hydrogen production but also efficiently degrading pollutants in wastewater, holding great promise for the simultaneous advancement of environmental protection and energy sustainability.[22–24]

Over the past few years, many electrocatalysts, especially those based on transition metals, have been employed to enhance the energy conversion efficiency of nitrogenous wastewater electrolysis (NWE), thereby emerging as enticing prospects for large-scale hydrogen generation.[25,26] However, the existing approaches often result in poor integration of NmOR and HER electrocatalysts in the same electrolyte due to electrode composition differences. Severe cross-contamination between electrodes during the electrocatalytic process may affect overall efficiency and selectivity. There is a pressing need to create bifunctional catalysts that can work on both the cathode and anode, lowering costs and simplifying system design.[14,27] The development of bifunctional transition metal-based catalysts for NWE systems has sparked widespread attention, giving a possible path to more efficient and economically feasible hydrogen production.

In this comprehensive review, we thoroughly investigated the most recent advancements in HWE systems, with an emphasis on the utilization of nitrogenous wastewater as a substrate for H_2 synthesis. To begin with, we summarized the key performance metrics for evaluating hydrogen generation from nitrogenous wastewater. These metrics encompass electricity consumption, energy-saving efficiency of hydrogen production, removal rate of nitrogenous pollutants, as well as selectivity and faradaic efficiency in nitrogenous contaminant removal. The corresponding measurement methods were also introduced in detail. Furthermore, we systematically classified and summarized various transition metal-based bifunctional catalysts for HER and NmOR. Through a focused review of representative works, the unique advantages and inherent limitations of different types of catalysts were elucidated. Lastly, the difficulties and challenges associated with bifunctional electrocatalysts for alternative NmOR were pointed out, with the goal of expediting the exploration of NWE for low-voltage H_2 production and pollutant degradation. Our review offers invaluable insights for the future development of bifunctional transition-metal catalysts, paving the way for energy-efficient hydrogen production in wastewater treatment.

2. Key performance metrics for assessing hydrogen generation from nitrogenous wastewater

The efficacy of energy-efficient hydrogen generation from nitrogenous wastewater is generally determined by a bifunctional electrocatalyst's capacity to catalyze hydrogen evolution at the cathode and the oxidation of nitrogenous compounds at the anode.[28] Beyond the conventional assessment parameters like overpotential, Tafel slope, turnover frequency (TOF), and catalyst stability, additional critical performance metrics must be considered for such bifunctional catalysts. These encompass the electrical energy consumption and the resultant energy-saving efficiency in hydrogen production, the rate of nitrogenous pollutant removal, and the selectivity coupled with

Yue Zhou

Yue Zhou is an associate professor in the College of Energy Storage Technology at the Shandong University of Science and Technology. She received her BS degree from Nankai University in 2011 and obtained her PhD degree in 2017 at Tianjin University. Her research interests mainly focus on advanced materials, in situ technologies, and simulation analysis for water/seawater electrocatalysis.

Liang Zhang

Liang Zhang graduated from Changzhou Institute of Technology in 2022 with a Bachelor of Engineering degree. He is currently pursuing his master's degree at Shandong University of Science and Technology under the supervision of Dr Yue Zhou. His research interests mainly focus on the design and construction of non-precious metal-based nanomaterials and their applications in electrochemical reactions.

Xin Yang

Prof. Xin Yang is currently the Vice Dean of the College of Energy Storage Technology at Shandong University of Science and Technology. He obtained both his Bachelor's and PhD degrees from Sichuan University. His primary research interests include solid oxide batteries/electrolytic cells and optoelectronic materials and devices. He has been recognized as an innovative talent in short supply by the Qingdao West Coast New District.

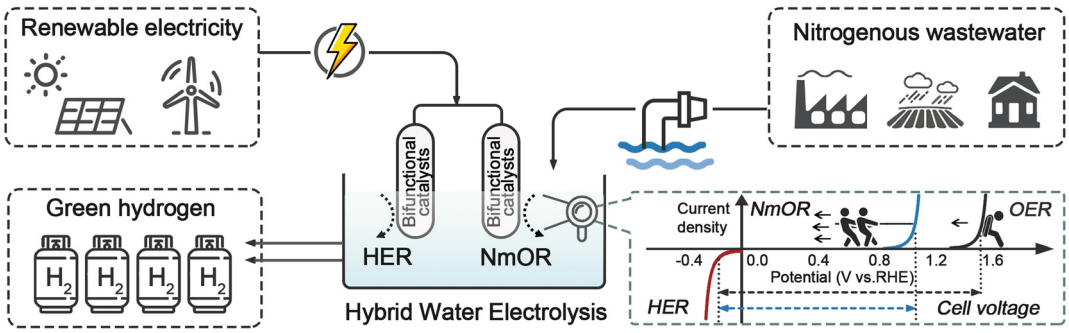

Fig. 1 Schematic of H_2 generation from renewable energy-powered HWE systems in nitrogenous wastewater.

faradaic efficiency (FE) in the removal of nitrogenous contaminants. These metrics are elaborated upon in the following sections.

2.1 Electricity consumption and energy saving efficiency of hydrogen production

The anodic reactions involving urea oxidation (UOR), hydrazine oxidation (HzOR), and ammonia oxidation (AmOR) are characterized by lower theoretical thermodynamic potentials relative to the OER.[28] This feature enables a notable decrease in the cell voltage required for hydrogen production from nitrogenous wastewater, as opposed to that from pure water. As a consequence, the electrolytic process for hydrogen generation becomes more efficient, with reduced energy consumption and enhanced energy conversion efficiency. To quantitatively evaluate the benefits of bifunctional catalysts in conserving energy during hydrogen production, it is essential to measure and calculate the electrical energy expended for hydrogen generation in nitrogenous wastewater and contrast it with that in pure water systems to ascertain the savings in electricity consumption.[29]

The total electrical energy consumption for hydrogen production is determined using the equation:

$$W = I \times \int U \mathrm{d}t \quad (1)$$

Here, W denotes the total electrical energy consumption, I represents the current of the electrolyzer, U is the voltage of the electrolyzer, and t signifies the reaction time.

The volume of hydrogen produced is computed based on the equation:

$$V = 22.4 \times I \times t/(Z \times F) \quad (2)$$

In this equation, V is the volume of produced hydrogen, Z is the number of electrons transferred (with a value of 2 for HER), and F is the Faraday constant (96 485 C mol^{-1}).

According to the results mentioned above, the basic electrical energy cost for hydrogen production is calculated as:

$$Q = W/V \ (\mathrm{kW\ h\ m^{-3}\ H_2}) \quad (3)$$

2.2 Removal rate of nitrogenous pollutants

The removal rate of nitrogenous pollutants is closely correlated with the reaction rate of the anodic catalyst in UOR, HzOR, or AmOR, serving as a key indicator of the catalyst's capability to treat nitrogenous wastewater. Taking the degradation of urea-rich wastewater as an example, urea degradation is measured using the modified diacetyl monoxime method.[30] By employing the prepared catalysts as the anode and cathode, and utilizing KOH solution mixed with urea as the electrolyte, the urea degradation system is operated under a constant voltage. Samples of the remaining urea solution are collected every fixed time interval, and the rate of urea degradation is subsequently determined using UV spectrophotometry.

2.3 Selectivity and faradaic efficiency in nitrogenous contaminant removal

Considering the multiple reaction pathways potentially involved in anodic UOR, HzOR, and AmOR, further exploration of the anodic products and mechanisms for energy-saving hydrogen production is warranted. Research over the past decades has largely centered on reducing the oxidation potential and increasing the oxidation current density. However, accurately identifying and analyzing the products remains challenging. For example, most studies on anodic UOR catalysts assume a "carbonate" pathway, which produces N_2 and CO_2 as the primary products. Nevertheless, recent studies have shown that nickel-based catalysts often follow a "cyanate" pathway, oxidizing urea to nitrites (NO_2^-), nitrates (NO_3^-), and toxic isocyanate (NCO^-), in addition to minor amounts of CO and N_2O. This results in N_2 selectivity below 55%.[31] These by-products may cause secondary environmental pollution but can also be coupled with H_2 production to achieve higher current densities. To selectively convert urea to N_2 during electrochemical UOR, cleavage of the C═N bond should be avoided. This can be achieved by donating electrons to the terminal oxygen atom of the C═O group, thereby increasing electron accumulation on the resonant C═N bond. Zhang's group reported that atomically isolated asymmetric Ni–O–Ti sites, with oxygenophilic Ti adjacent to Ni, favor interaction with the carbonyl group over the amino group in urea. This prevents premature cleavage of the resonant C═N bond before

intramolecular N–N coupling, achieving an N_2 selectivity of up to 99%.[32] Moreover, the proximity of the oxidation potentials between the OER and UOR leads to intense competition.[33] Therefore, in addition to the removal rate of nitrogenous pollutants, the selectivity of products and faradaic efficiency in anodic UOR, HzOR, and AmOR reactions must be accorded high priority. A combination of ion chromatography and in-line gas chromatography analysis serves as an effective means to determine the FE of N_2 and NO_x^- during the electrolysis process.

3. Electrocatalytic oxidation of various nitrogenous substances coupled with HER

Substantial amounts of nitrogenous wastewater, including urea, hydrazine, and ammonia, are emitted from industrial operations, daily living, and agricultural activities, causing serious environmental and health issues. Traditionally, wastewater treatment has relied on chemical or enzymatic reactions, often requiring harsh conditions or high costs.[34,35] While microbial decomposition has emerged as a more cost-effective solution, the concurrent conversion of wastewater into energy offers the added advantages of energy conservation and broad applicability.[36,37] Lately, the electrocatalytic treatment of wastewater has become a prominent strategy due to its efficiency and eco-friendliness. The thermodynamically favorable oxidation of nitrogenous compounds coupled with the cathodic HER in HWE systems, shows great potential for energy-efficient hydrogen generation and environmental sustainability (Fig. 2).[38,39] However, there is an urgent need for highly efficient electrocatalysts to mitigate the substantial overpotential associated with multiple electron-transfer steps. The following sections give a thorough examination of transition-metal-based bifunctional electrocatalysts, which are pivotal in enhancing the electrocatalytic oxidation of wastewater pollutants in alkaline media.

3.1 Urea

Large-scale utilization of urea as a crucial source of nitrogen is prevalent in both industrial and agricultural sectors. However, there is an imperative need for appropriate treatment of urea-containing wastewater because of the increasing severity of water pollution caused by discharge.[40,41] It has been reported that substituting the OER with the UOR can effectively reduce the theoretical overpotential of water splitting. Specifically, while the OER requires a thermodynamic potential of 1.23 V, the UOR only necessitates 0.37 V.[42] Thus, urea-assisted water electrolysis not only facilitates the degradation of urea-rich wastewater but also conserves energy for hydrogen production, holding substantial implications for energy provision and global environmental concerns. The reactions for urea-assisted water splitting are as follows:

$$\text{Anode reaction: } CO(NH_2)_2 + 6OH^- \rightarrow N_2 + 5H_2O + CO_2 + 6e^- \quad (4)$$

$$\text{Cathode reaction: } 6H_2O + 6e^- \rightarrow 3H_2 + 6OH^- \quad (5)$$

3.1.1 Ni-based catalysts. Although the urea-assisted electrolysis system offers a lower theoretical energy requirement, the slow kinetics of the UOR, involving a complex six-electron transfer process, hinder the overall reaction efficiency.[43] To address this, the development of highly efficient bifunctional catalysts has become a focal point. Nickel is widely recognized for its superior electrochemical activity in both urea oxidation and hydrogen evolution, rendering Ni-based catalysts particularly effective. Ni-based catalysts, which are the most extensively researched, exhibit an initial oxidation of low-valent surface nickel species to NiOOH as the potential increases. Urea is then oxidized by NiOOH to produce N_2, CO_2, and H_2O, while NiOOH is concurrently reduced back to Ni^{2+} species.[43] During this process, byproducts such as NH_4^+ or NO_x^- may form, presenting significant challenges for practical applications.[44] A variety of Ni-based catalysts, including Ni–S–Se/NF, Ni@NCNT, and Fe–Ni_3S_2, have demonstrated notable performance in both UOR and HER.[45–47]

Huang and colleagues developed a self-standing bifunctional catalyst, Ni-NC@DWC, by embedding lattice-deformed Ni nanoparticles within a nitrogen-doped carbon coating on

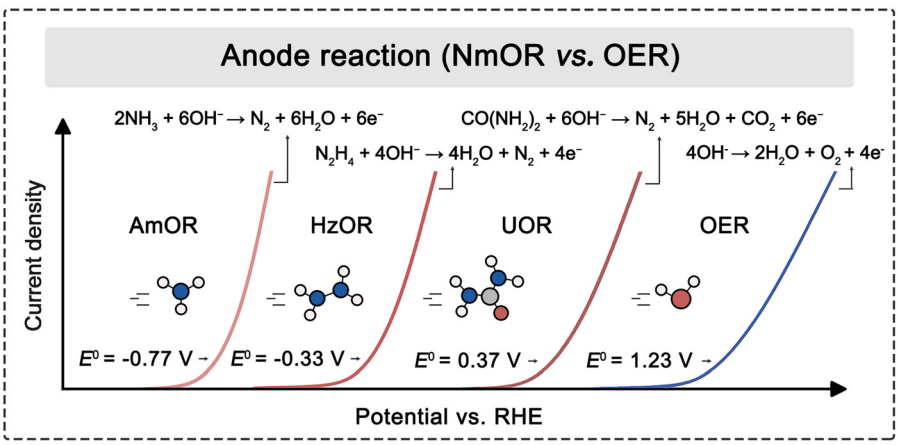

Fig. 2 Comparison of various electrocatalytic oxidation reactions of nitrogenous substances with the OER.

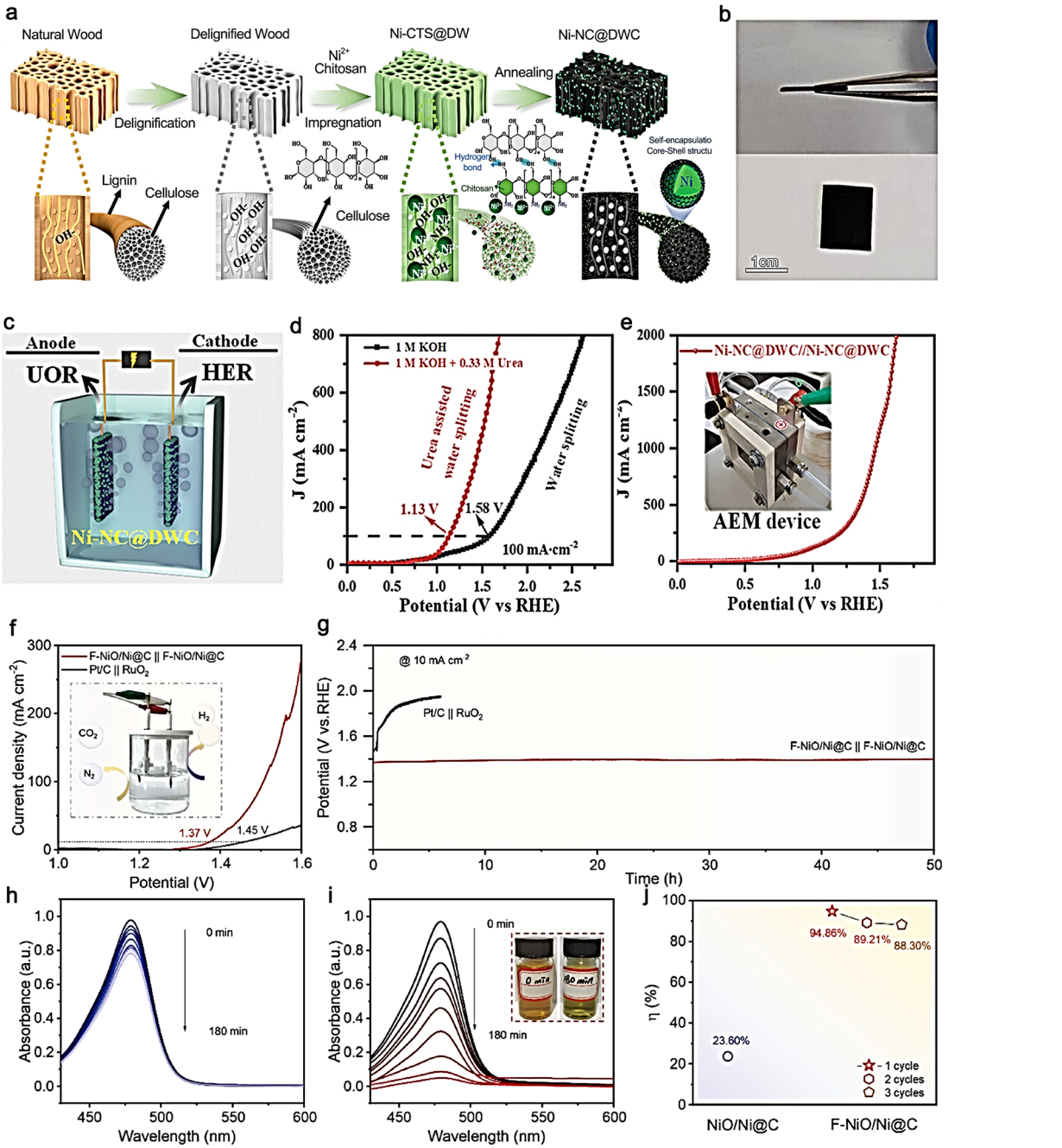

Fig. 3 (a) Synthesis process diagram of Ni–NC@DWC. (b) Photo of Ni–NC@DWC. (c) Installation diagram of urea-assisted water electrolyzer. (d) Water splitting and urea-assisted HWE performance of Ni–NC@DWC. (e) Polarization curves of Ni–NC@DWC||Ni–NC@DWC AEM electrolyzer.[48] Copyright 2024, Wiley-VCH. (f) LSV curves of F–NiO/Ni@C and RuO_2||Pt/C for urea-assisted HWE. (g) Stability tests of F–NiO/Ni@C and RuO_2||Pt/C at the current density of 10 mA cm^{-2}. UV-vis spectra of (h) NiO/Ni@C and (i) F–NiO/Ni@C during urea degradation. (j) Urea degradation values for F–NiO/Ni@C and NiO/Ni@C.[49] Copyright 2023, Wiley-VCH.

delignified wood carbon (Fig. 3(a) and (b)).[48] *In situ* FT-IR and Raman spectra, combined with theoretical calculations, indicated that lattice deformation, driven by strong metal–support interactions, enhances electron transfer and the adsorption/desorption of reaction intermediates, thereby boosting the efficiencies of both UOR and HER. Notably, the active site Ni^{3+}–O is continuously renewed during UOR. When deployed as a self-standing electrode in an alkaline electrolyte, Ni–NC@DWC demonstrated potentials of −24 mV for HER and 1.244 V for UOR at a current density of 100 mA cm^{-2}, highlighting its enhanced bifunctional performance. This UOR efficacy starkly diverges from the OER efficacy (1.607 V) under identical conditions. Furthermore, a two-electrode urea-assisted water electrolyzer incorporating Ni–NC@DWC achieved a current density of 100 mA cm^{-2} at an unusually low cell voltage of 1.13 V, with 100% faradaic efficiencies for

both H_2 and N_2 outputs, marking a substantial 450-mV decrease relative to conventional water splitting processes (Fig. 3(c)–(e)). The urea concentration in the electrolyzer also decreases over time, ultimately achieving a conversion rate close to ≈100%. In a recent investigation, Xu's team unveiled a fluorine-doped heterogenous catalyst, F–NiO/Ni@C, employed at both the anode and cathode in a urea-assisted water electrolysis setup.[49] The deliberate F-doping enhances electron delocalization and promotes electron transfer from Ni to NiO at the nano-scale interfaces. This interfacial collaboration furnishes readily available F–NiO active sites, permitting F–NiO/Ni@C to attain optimal H* adsorption Gibbs free energy for HER and a diminished energy barrier for UOR. As a result, this catalyst surpassed the benchmark $RuO_2||Pt/C$ cell, necessitating only 1.37 V to attain a current density of 10 mA cm^{-2} for urea-assisted water splitting (Fig. 3(f)). Moreover, the F–NiO/Ni@C catalyst displayed an admirable urea elimination rate of 94.86%, a striking 4.02-fold enhancement compared to the unmodified NiO/Ni@C (Fig. 3(g)–(j)).

To address the challenges posed by the spontaneous oxidation of Ni species and the formation of harmful liquid-phase byproducts (NO_x^-) from the over-oxidation of urea, Hou's research team engineered a self-supported, tungsten-doped nickel-based coordination polymer that functions as a bifunctional catalyst (W–NT@NF).[50] This novel catalyst was designed to boost both the activity and selectivity in urea-assisted water splitting processes. It exhibited dual functionality, with the ability to reach high current densities approaching 1000 mA cm^{-2} in both HER and UOR. Utilizing in-line gas chromatography and ion chromatography for a detailed analysis, it was found that the FE for N_2 production was significantly higher (34%) at lower current densities (<100 mA cm^{-2}), while the FE for NO_x^- maintained consistently below 20% during long-term electrolysis. Further insights were gained through *in situ* experiments complemented by density functional theory (DFT) computations, which highlighted that Ni^{3+} sites—resistant to self-oxidation—serve as the primary active sites, thereby promoting rapid kinetics in urea oxidation. Concurrently, W sites were found to interact synergistically with Ni sites, hastening the kinetics of HER and consequently refining the energy conversion efficiency in urea-assisted water electrolysis. This synergistic interplay between W and Ni not only amplifies the catalyst's overall performance but also secures its stability and operational efficiency over extended durations.

3.1.2 Co-based catalysts. Beyond the realm of nickel-based catalysts, high-valent cobalt species have risen to prominence as effective catalysts for enhancing urea electro-oxidation, thus expediting the electrocatalytic process. A prime example is the work by Song's group, who developed a porous amorphous cobalt hydroxysulfide core–shell nanoneedle catalyst on a titanium mesh, designated as P–$CoS_x(OH)_y$ NN/Ti.[51] These nanoneedles, marked by their high aspect ratio, are enveloped by a multitude of ultra-thin nanosheets. The amorphous and porous characteristics of the material, in conjunction with the nanosheets, yield a substantial specific surface area and a plethora of active sites. P–$CoS_x(OH)_y$ NN/Ti exhibits exceptional performance in the HER. Furthermore, the catalyst is replete with Co^{3+} ions and oxygen vacancies, which are advantageous for augmenting the UOR activity. When deployed in a two-electrode configuration, the electrolyzer functions at a mere 1.3 V to attain a current density of 10 mA cm^{-2}, effectively conserving energy by replacing the OER with UOR (Fig. 4(a)–(c)).

Following this, Pan *et al.* introduced a bifunctional Ni-modified Co_2VO_4 heterojunction mesoporous nanosheet catalyst supported on a nickel foam (NF) substrate (Ni–Co_2VO_4/NF).[53] Utilizing a two-electrode setup with 1 M KOH and 0.5 M urea as the electrolyte, this catalyst achieved a current density of 10 mA cm^{-2} at a relatively low voltage of 1.36 V. Moreover, it sustained stable operation at 500 mA cm^{-2} for 140 hours with negligible loss of activity, underscoring its suitability for efficient urea wastewater treatment and hydrogen production. The heightened activity is ascribed to the robust heterojunction between Ni and Co_2VO_4, which modulates the interfacial electronic structure to create electron-deficient/rich species that facilitate H_2O/urea adsorption and enhance intrinsic HER/UOR activity. Additionally, the mesoporous nanosheet structure, characterized by its expansive specific surface area, exposes a greater number of active sites and aids in the desorption of bubbles on the electrode surface, thereby boosting HER/UOR reaction kinetics and stability at elevated current densities. In another study, Hao's group reported a strongly coupled heterostructured CoP/MoO_2 catalyst for urea-assisted water splitting.[54] Benefiting from the synergistic effect and strong electronic interactions between CoP and MoO_2, this catalyst required low potentials of −0.011 V and 1.26 V to achieve a current density of 10 mA cm^{-2} for HER and UOR, respectively. When applied in a urea-assisted water electrolyzer, CoP/MoO_2 reached 10 mA cm^{-2} at only 1.32 V, significantly lower than the Pt/C||RuO_2 benchmark, while also exhibiting robust stability. Overall, the heterostructured CoP/MoO_2 offers an effective and energy-saving approach for urea-assisted hydrogen production.

3.1.3 Multiple transition-metal catalysts. In the realm of urea electro-oxidation, three pivotal issues necessitate resolution: the interaction between urea and the catalyst, the activation of C–N bonds within the urea molecule, and the deactivation of active sites by molecular fragments.[31] A multimetallic transition-metal system is anticipated to deliver substantial enhancements in these critical areas. Recently, catalysts incorporating multiple transition metals, such as those based on NiCo, have been engineered to enhance bifunctional performance in both the UOR and the HER.[52,53] A case in point is the synthesis of porous phosphorized $CoNi_2S_4$ yolk–shell spheres (P–$CoNi_2S_4$ YSSs) *via* a dual-process approach involving hydrothermal sulfidation and gas-phase phosphorization.[55] The enhanced electronic conductivity, bolstered Ni^{3+}/Ni^{2+} redox couple, and hollow morphology of P–$CoNi_2S_4$ YSSs contribute to their superior activity and durability in alkaline media, achieving low potentials of −0.135 V for HER and 1.306 V for UOR at a current density of 10 mA cm^{-2}. Notably, when used as both anode and cathode, the P–$CoNi_2S_4$

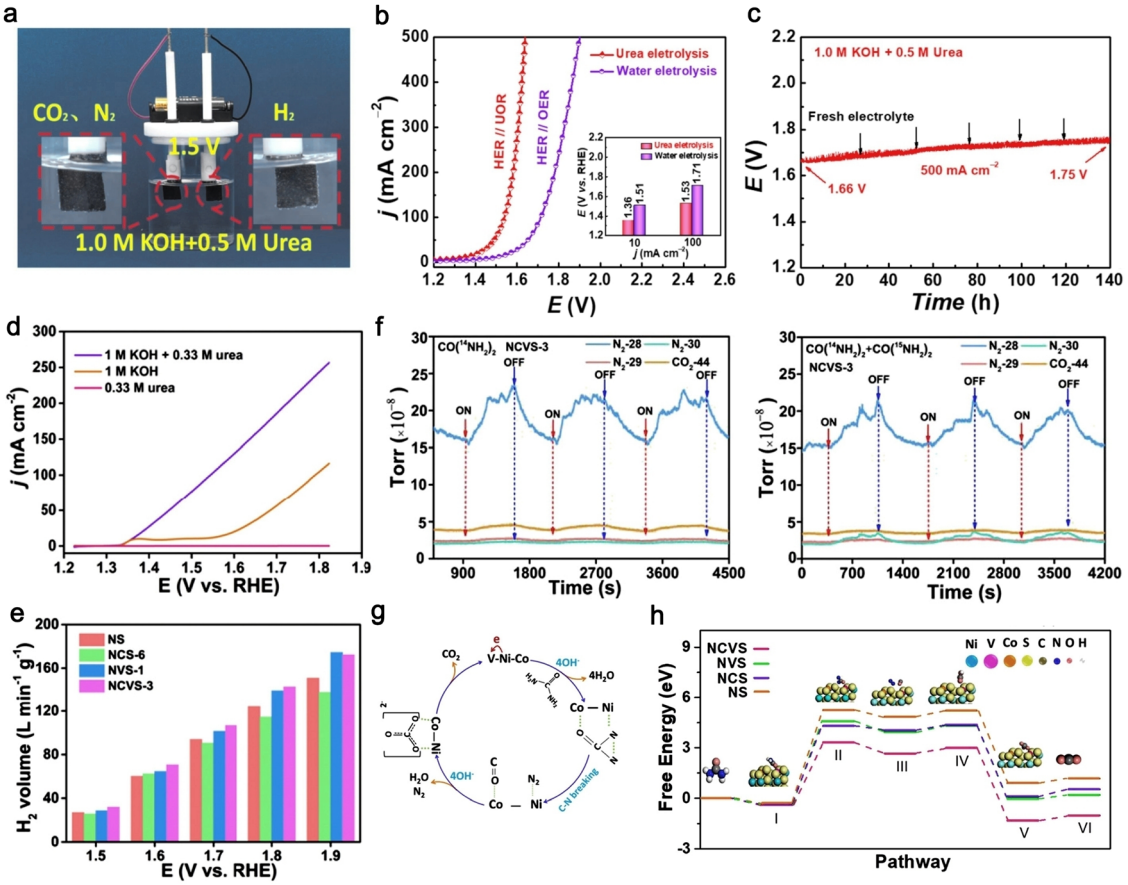

Fig. 4 (a) Ni–Co_2VO_4/NF for HER||UOR electrolyzer drived by a 1.5 V battery. (b) LSV curves of Ni–Co_2VO_4/NF for urea and water electrolysis. (c) Stability test at 500 mA cm^{-2} for 140 h.[51] Copyright 2021, Royal Society of Chemistry. (d) LSV curves of NCVS-3 in 1 M KOH + 0.33 M urea, 1 M KOH, and 0.33 M urea. (e) Hydrogen production rate of different catalysts in 1 M KOH + 0.33 M urea. (f) *In situ* electrochemical mass spectrometry isotope tracing experiment of NCVS-3. (g) UOR mechanism of NCVS-3. (h) Gibbs free energy profiles of UOR on NCVS, NVS, NCS, and NS.[52] Copyright 2022, American Chemical Society.

catalyst necessitates a mere cell voltage of 1.402 V in urea electrolysis to achieve 10 mA cm^{-2}, a reduction of 142 mV compared to water splitting requirements. Expanding beyond binary NiCo-based catalysts, Hu's team devised a Co, V co-doped NiS_2 ternary system to facilitate energy-efficient urea-assisted hydrogen production.[52] The optimal ternary catalyst exhibited robust urea electro-oxidation activity, with a current density of 77 mA cm^{-2} at 1.5 V and hydrogen generation of 143 L min^{-1} g_{cat}^{-1} at 1.8 V (Fig. 4(d) and (e)). Advanced characterization methods, encompassing X-ray photoelectron spectroscopy, *in situ* electrochemical mass spectrometry isotope tracing, *in situ* electrochemical Raman spectroscopy, and DFT analyses, unveiled that the extended superexchange interaction not only intensified electron transfer between Ni and S but also hastened electron exchange between urea and the catalyst (Fig. 4(f)–(h)). Anti-CO poisoning tests indicated that the existence of Co expedited the oxidation of carbonaceous intermediates, thereby bolstering catalyst stability. Significantly, N_2 formation was observed to occur *via* the urea intermolecular N–N coupling process catalyzed by metal sulfides, offering profound insights into UOR catalysis by metal sulfides.

Recently, other multicomponent materials, including $NiMoO_4$, NiFe MOF, and NiFe LDH, have been synergized with Ru to further enhance their bifunctional UOR and HER capabilities.[56,57] For instance, Wang and colleagues adopted a simple strategy of V cation doping coupled with Ru nanoparticle modification to fabricate a multifunctional NiFe-LDH electrocatalyst (Ru/V–NiFe-LDH) on a NF substrate.[57] This Ru/V–NiFe-LDH/NF catalyst displayed remarkable catalytic activity and stability in both HER and UOR, markedly surpassing commercial Pt/C and RuO_2 catalysts. The exceptional electrochemical attributes primarily emanate from V doping and Ru nanoparticle modification, which altered the surface charge state of the NiFe-LDH matrix, prompting electron rearrangement, expediting charge transfer, augmenting active sites, and enhancing intrinsic catalytic activity. When integrated into a two-electrode system for overall urea splitting, a low cell voltage of 1.40 V at 10 mA cm^{-2} was attained, a decrease of 130 mV relative to water splitting. Moreover, the system demonstrated remarkable stability, with only a 19% decline in high current density at 50 mA cm^{-2} after 48 hours. This research underscores the significance of judicious design in crafting

high-performance multifunctional electrocatalysts for overall urea splitting applications.

3.2 Hydrazine

Hydrazine, a vital industrial chemical, is extensively utilized in applications such as rocket propellants and fuel cells.[58,59] However, its emissions pose significant and long-lasting environmental challenges due to its high toxicity. Similar to urea, hydrazine offers multiple advantages for hydrogen production *via* hydrazine-assisted water electrolysis. Incorporating HzOR into hybrid water electrolysis systems not only mitigates hydrazine-related pollution but also leverages the thermodynamically favorable process of hydrazine oxidation (−0.33 V) to substantially reduce the energy input for hydrogen generation.[60,61] More importantly, compared to the narrow oxidation potential window between UOR and OER, the potential window between HzOR and OER is significantly expanded, effectively reducing adverse competition from OER. These benefits have spurred intensive research into HzOR for efficient hydrogen production. In hydrazine-assisted water splitting, the anodic reaction can be represented as follows:

$$\text{Anode reaction: } N_2H_4 + 4OH^- \rightarrow 4H_2O + N_2 + 4e^- \quad (6)$$

3.2.1 Ni-based catalysts. The coupling of HzOR and HER on transition-metal catalysts, particularly nickel-based bifunctional materials, has garnered increasing attention in recent years due to the multi-electron transfer process involved.[62–64] Yang and associates introduced a self-supported heterostructure catalyst, $Ni(OH)_2/Ni_2P$, which exhibits remarkable efficacy in hydrogen production from hydrazine solutions (Fig. 5(a)).[65] This catalyst operates at a minimal potential of 0.357 V to attain a current density of 100 mA cm^{-2}, a substantial decrease compared to the 1.89 V necessary for the OER, and sustains stable electrolysis for a full 24-hour period. Wang *et al.* engineered P and Fe co-doped $NiSe_2$ ultrathin nanosheets on NF, which display exceptional bifunctional catalytic performance for both HzOR and HER.[66] This P/Fe–$NiSe_2$ catalyst achieves a current density of 100 mA cm^{-2} at notably low potentials of 200 mV for HzOR and −168 mV for HER. Drawing on electrochemical studies, *in situ* characterizations, and DFT computations, a propitious "2 + 2" reaction mechanism entailing a two-step HER and a two-step HzOR was conclusively established. When applied in a hydrazine-assisted water splitting configuration, the voltage requisite to propel a current density of 100 mA cm^{-2} was significantly reduced by roughly 1.3 V in contrast to the conventional water electrolyzer, highlighting the prospect for energy-efficient hydrogen production from hydrazine solutions (Fig. 5(b) and (c)).

Traditionally, anodic HzOR is understood to involve a four-proton-coupled electron transfer step, accompanied by the sequential dehydrogenation of hydrazine to nitrogen.[68,69] However, a more kinetically advantageous two-step two-electron mechanism has recently been discovered, promising to accelerate the kinetics of hydrazine-assisted water splitting for efficient hydrogen generation and wastewater treatment. As revealed by Sun *et al.*, the Ni(Cu) CNPs catalyst exhibits exceptional electrocatalytic performance for both HzOR and HER.[67] This hybrid system is capable of delivering a current density of 200 mA cm^{-2} at a cell voltage of 0.527 V, marking a significant reduction of 1.62 V compared to OWS, indicative of a substantial decrease in energy consumption (Fig. 5(d)–(f)). This remarkable catalytic performance is attributed to a two-stage electron transfer process, which begins with a slow two-electron transfer to form diazene as an intermediate, followed by a second two-electron transfer to produce nitrogen gas (Fig. 5(g)–(i)).

3.2.2 Co-based catalysts. Cobalt-based materials have risen to prominence as superior bifunctional electrocatalysts, adept at catalyzing both the HzOR and the HER. Xia *et al.* introduced a bifunctional tubular cobalt perselenide ($CoSe_2$) nanosheet electrode for electrochemical hydrogen production, assisted by anodic hydrazine oxidation in water electrolysis (Fig. 6(a)).[58] The fabricated $CoSe_2$ electrode exhibits potentials of −84 mV for HER and −17 mV for HzOR, respectively, to achieve a current density of 10 mA cm^{-2}. Furthermore, an exceptionally low cell voltage of merely 164 mV is sufficient to sustain a current density of 10 mA cm^{-2} over 14 hours of stable water electrolysis, markedly surpassing the theoretical voltage for water splitting (Fig. 6(b)).

The heterojunction engineering of cobalt-based catalysts has been reported to induce interfacial electric fields, facilitating electronic state reconfiguration along the engineered heterointerface, thereby enhancing the bifunctional performance in HzOR and HER. For instance, Huang's team presented an integrated catalyst, CoH-CoP_V@CFP, comprising amorphous $Co(OH)_2$ nanosheets and CoP.[70] DFT calculations revealed that electron-deficient cobalt sites in $Co(OH)_2$ exhibit strong N–Co interactions, which accelerate N_2H_4 dehydrogenation kinetics. Meanwhile, phosphorus vacancies in CoP critically modulate H* adsorption energy, thus attaining exceptional bifunctionality. This catalyst manifests low overpotentials of −77 mV and −61 mV at 10 mA cm^{-2} for HER and HzOR in alkaline media, respectively. As a result, the strategic coupling of HzOR and HER permits hydrogen evolution at a minimal cell voltage of 0.23 V to attain 500 mA cm^{-2}, underscoring the potential for energy-efficient H_2 synthesis and hydrazine treatment (Fig. 6(c) and (d)).

In a bid to facilitate the outdoor application of hydrazine splitting, Fe-doped CoS_2 nanosheets have been developed as a bifunctional electrocatalyst for self-powered H_2 production, integrating direct hydrazine fuel cells with overall-hydrazine-splitting units (Fig. 6(e)).[71] This system innovatively employs hydrazine in a dual capacity—as the fuel for direct hydrazine fuel cells and as the target for splitting—achieving an H_2 evolution rate of 9.95 mmol h^{-1} (Fig. 6(f)), a faradaic efficiency of 98%, and 20-hour stability, all of which are on par with the best-reported self-powered water splitting systems. Theoretical calculations indicate that Fe doping reduces the free-energy changes associated with H adsorption and NH_2NH_2* dehydrogenation on CoS_2, accounting for the observed high-performance outcomes (Fig. 6(g)).

3.2.3 Rh-based catalysts. Transition metals like Ni and Co, along with their nanomaterial derivatives, are deemed

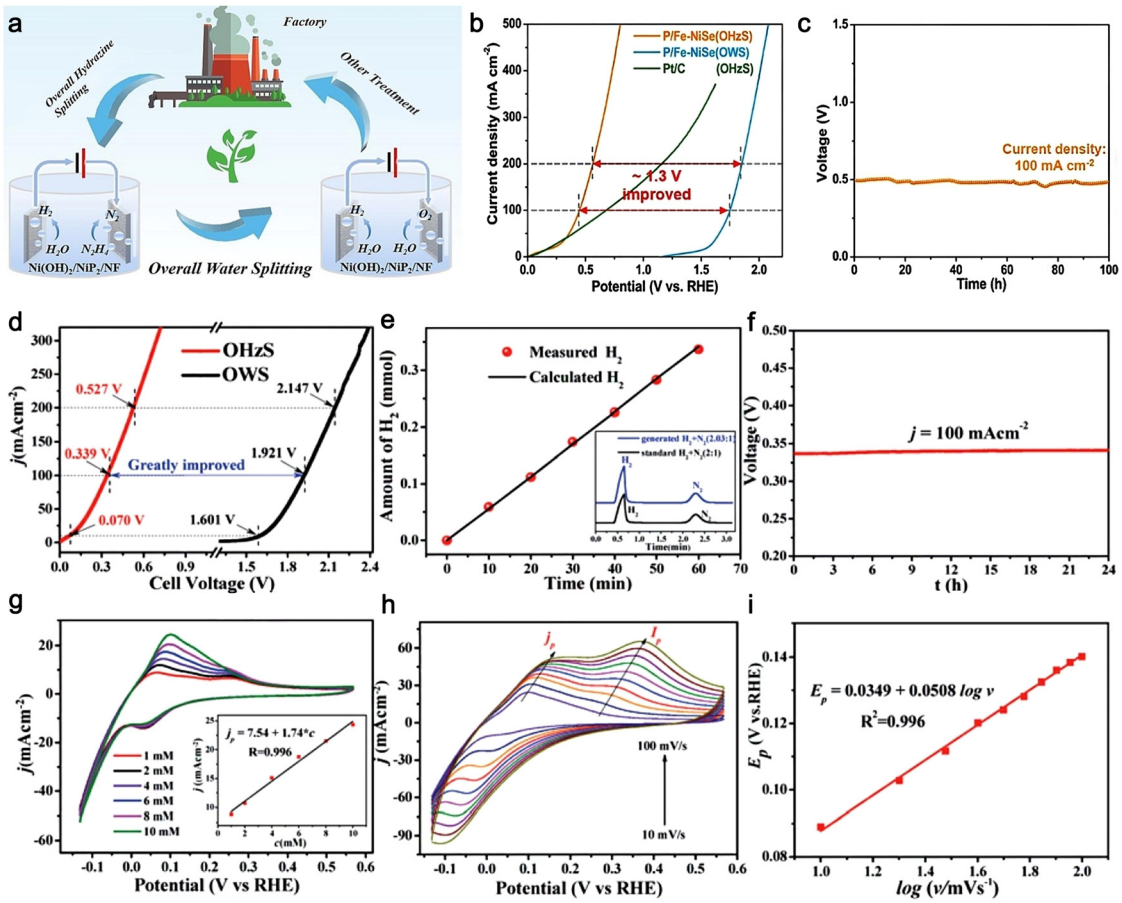

Fig. 5 (a) Scheme for $Ni(OH)_2/Ni_2P$/NF in an eco-friendly cycle.[65] Copyright 2023, Elsevier. (b) Polarization curves of P/Fe–$NiSe_2$ for hydrazine-assisted water splitting. (c) Durability of P/Fe–$NiSe_2$ at 100 mA cm^{-2}.[66] Copyright 2023, Springer Nature. (d) Electrocatalytic performance of Ni(Cu) CNPs catalyst in hydrazine-assisted water electrolyzer and OWS. (e) The quantity of theoretical and observed H_2 production. (f) Durability test of Ni(Cu) CNPs in a hydrazine-assisted water electrolyzer. (g) CV curves of Ni(Cu) CNPs in 1 M KOH solution with different concentrations of hydrazine, insert is the calibration curve of peak current *vs.* hydrazine concentration. (h) CV curves of Ni(Cu) CNPs obtained in the solution of 1 M KOH + 10 mM hydrazine at different scan rates. (i) Plot of HzOR peak potential E_p against log(v).[67] Copyright 2020, Royal Society of Chemistry.

prospective bifunctional electrocatalysts for HzOR and HER, attributed to their affordability and notable electrocatalytic activity in alkaline conditions. However, the inescapable formation of metal oxide layers on the surface of non-noble metal-based nanomaterials during HzOR precipitously decreases their reactivity, thereby significantly hampering their commercial viability. At present, platinum (Pt) group metals remain the preferred HzOR/HER bifunctional electrocatalysts for practical applications, given their elevated activity and robust stability. Among these, rhodium (Rh), a well-known noble metal, manifests high catalytic activity across numerous pivotal industrial processes.[72] To further enhance performance, endeavors have been concentrated on tailoring the morphology and interface of these catalysts, which are pivotal for modulating the active sites and electronic configuration. For example, Jia and associates utilized porous nitrogen-doped carbon nanobowls (N-CBs) to controllably grow ultrafine Rh nanoparticles.[73] Leveraging the interfacial bond between Rh and nitrogen, ultrafine Rh nanoparticles averaging 1.4 nm in size were successfully anchored onto the N-CBs. This Rh/N-CB electrocatalyst exhibits remarkable activity, with overpotentials of 72 mV for HzOR and 77 mV for HER to achieve a current density of 10 mA cm^{-2}. More importantly, the Rh/N-CB catalyst serves as an efficacious electrode for hydrogen generation in a 1 M KOH solution mixed with 0.5 M N_2H_4, yielding a current density of 20 mA cm^{-2} at a mere 0.2 V electrolysis voltage, indicative of high energy conversion efficiency.

Recently, Rh/RhO_x nanosheets have been engineered to function as bifunctional catalysts for HER and HzOR across the entire pH range.[74] Through a strong alkali-assisted thermosynthesis followed by hydrogen reduction, small Rh nanoparticles are *in situ* grown on RhO_x nanosheets, providing a tight interfacial interaction between the metal and oxide, thereby modulating the chemical states of Rh (Fig. 7(a) and (b)). In the fabrication of water splitting devices, the optimal Rh/RhO_x-500 catalyst necessitates cell voltages of 0.068 V, 0.268 V, and 0.348 V to attain a current density of 10 mA cm^{-2} in 1.0 M KOH, 1.0 M PBS, and 0.5 M H_2SO_4 electrolytes, respectively, each supplemented with a certain concentration of N_2H_4 (Fig. 7(c)). DFT calculations suggest that the

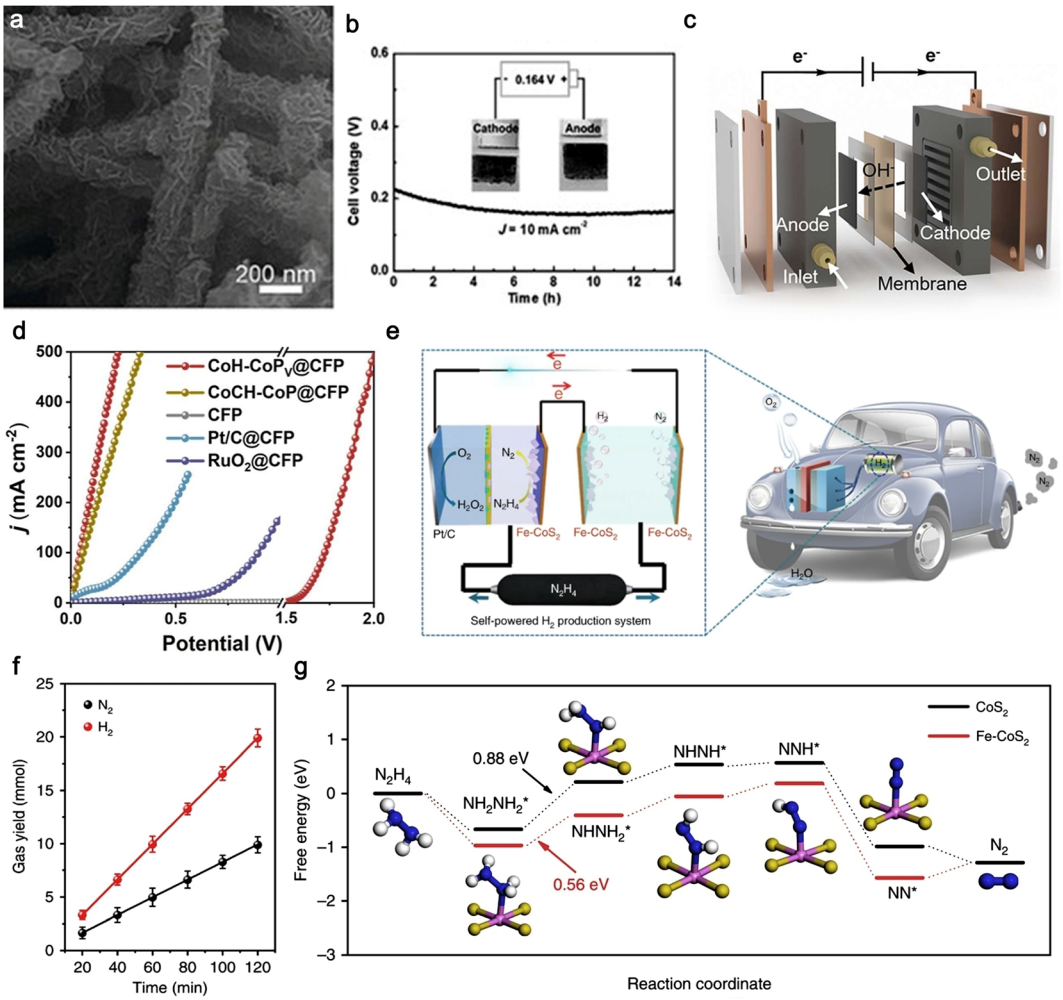

Fig. 6 (a) SEM image of tubular $CoSe_2$ nanosheets. (b) Stability test of $CoSe_2$||$CoSe_2$ couple in 1 M KOH + 0.5 M N_2H_4.[58] Copyright 2018, Wiley-VCH. (c) Schematic illustration of AEM electrolyzer. (d) LSV curves CoH-CoP_V@CFP.[70] Copyright 2024, Elsevier. (e) Scheme of a self-powered hydrogen production system with Fe–CoS_2 as the catalyst. (f) Gas yield of N_2 and H_2 in the system. (g) Gibbs free energy profiles of HzOR on Fe–CoS_2 and CoS_2.[71] Copyright 2018, Springer Nature.

incorporation of the Rh/RhO_x interface activates the surface Rh and reduces the reaction energy barrier, leading to the exceptional performance of the Rh/RhO_x-500 catalyst.

Typically, bimetallic noble metal nanomaterials exhibit superior electroactivity compared to their monometallic counterparts, owing to synergistic interactions. Taking into account the intrinsic chemical attributes of Au nanomaterials, ultrafine Au@Rh core–shell nanowires (Au@Rh ultra-NWs) were synthesized to improve bifunctional HzOR and HER performance.[72] Experimental assessments and theoretical calculations corroborated that the introduction of the Au ultra-NWs core enhanced the electrocatalytic activity and stability of Rh for HzOR and HER, stemming from the interplay between Au and Rh. Under illumination, Au@Rh ultra-NWs further displayed plasma-enhanced electrocatalytic activity for HzOR. The experimental findings first indicated that both photoelectric and photothermal effects were instrumental in the plasma-enhanced electrocatalytic activity of Au@Rh ultra-NWs. Recently, Duan's group reported the synthesis of ultrathin $RhRu_{0.5}$-alloy wavy nanowires as bifunctional electrocatalysts for HzOR and cathodic HER.[75] These $RhRu_{0.5}$-alloy wavy nanowires accomplish complete electrooxidation of hydrazine with a low overpotential and high mass activity, alongside enhanced HER performance. The resultant $RhRu_{0.5}$ bifunctional electrocatalysts facilitate high-performance hydrazine-assisted water electrolysis, delivering a high current density of 853 mA cm^{-2} at a cell voltage of 0.6 V, and sustaining stable operation at a high current density of 100 mA cm^{-2} for 80 hours with minimal irreversible degradation (Fig. 7(d) and (e)). The overall performance markedly surpasses that of previously documented hydrazine-assisted water electrolyzers, presenting a viable route for efficiently converting hazardous hydrazine into molecular hydrogen.

3.2.4 Ru-based catalysts. Compared to Rh-based catalysts, Ru-based catalysts, which are more cost-effective within the Pt-group materials, have been reported to exhibit enhanced bifunctional performance in both HzOR and HER. Zhang's group introduced a rationally designed synthesis of partially

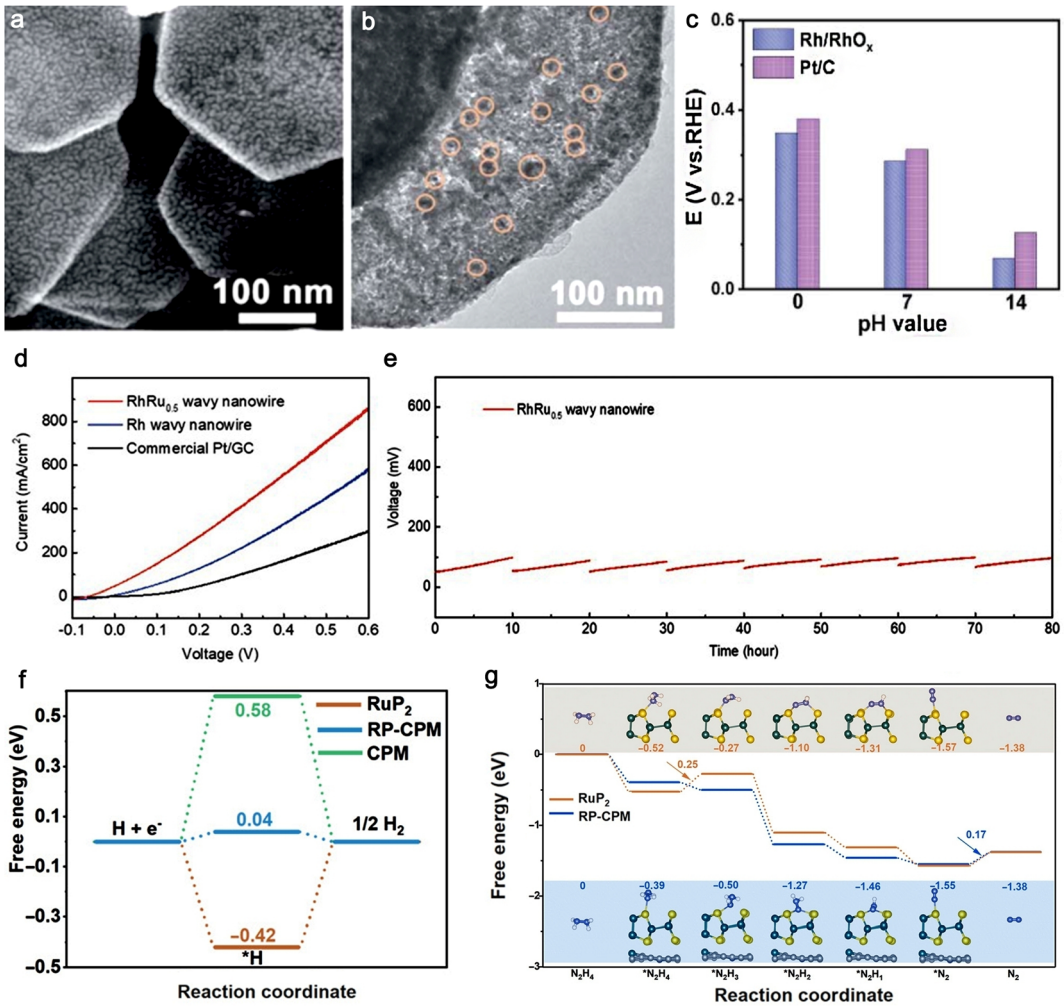

Fig. 7 (a) SEM and (b) TEM images of Rh/RhO$_x$-500. (c) Performance comparison of Rh/RhO$_x$-500 and Pt/C at different pH.[74] Copyright 2022, Royal Society of Chemistry. (d) LSV curves of RhRu$_{0.5}$ wavy nanowire and comparison samples for hydrazine-assisted water splitting. (e) Stability test of RhRu$_{0.5}$ wavy nanowire for 80 h.[75] Copyright 2023, Wiley-VCH. (f) Gibbs free energy profiles of HER on RP-CPM and comparison samples. (g) Gibbs free energy changes and corresponding reaction pathways of HzOR on RP-CPM and RuP$_2$.[76] Copyright 2020, The American Association for the Advancement of Science.

exposed RuP$_2$ nanoparticle-decorated N, P dual-doped carbon porous microsheets (referred to as RP-CPM), employing a scalable one-pot approach.[76] This catalyst necessitates an exceedingly small working potential of −70 mV to achieve a current density of 10 mA cm^{-2} for HzOR in a 1 M KOH + 0.3 M N_2H_4 solution and exhibits an exceptionally low overpotential of 24 mV at 10 mA cm^{-2} for HER in 1 M KOH. Notably, a record-low cell voltage of 23 mV is required to attain a current density of 10 mA cm^{-2} in a two-electrode system for overall hydrazine splitting (OHzS), with the capability of reaching an ultrahigh current density of 522 mA cm^{-2} at a modest cell voltage of 1.0 V. Furthermore, the extended application of RP-CPM as an anode catalyst in direct hydrazine fuel cells (DHzFC) was demonstrated, achieving a respectable power density of 64.77 mW cm^{-2} in a 1 M KOH + 0.5 M N_2H_4 electrolyte at ambient temperature. Leveraging this exceptional performance, a hydrogen production system powered by DHzFC and OHzS was showcased, achieving a promising H_2 generation rate of 0.68 mmol h^{-1} at room temperature with a relatively low hydrazine concentration. DFT calculations revealed that the C sites in RP-CPM exhibit more moderate hydrogen absorption kinetics for HER, while the active Ru sites in the hybrid structure possess more favorable dehydrogenation kinetics compared to pure RuP$_2$ for HzOR, highlighting the significance of the partially exposed RuP$_2$ surface (Fig. 7(f) and (g)).

To further enhance the utilization and mass activity of Ru-based catalysts, ruthenium single atoms (Ru SAs) anchored onto sulfur-vacancies of WS_2 were prepared utilizing a sulfidation and straightforward galvanostatic deposition method.[77] The WS_2/Ru SAs function as a bifunctional catalyst, achieving ultralow potentials of −74 mV and −32.1 mV at 10 mA cm^{-2} for HzOR and HER, respectively. When used in a two-electrode electrolyzer, WS_2/Ru SAs reach a current density of 10 mA cm^{-2} with a cell voltage of merely 15.4 mV, significantly lower than most electrocatalysts. DFT calculations elucidate the pivotal role of Ru SAs in WS_2, where the sluggish dissociation of water

in HER is facilitated at Ru sites, and the sulfur sites of WS_2 exhibit more moderate behavior for hydrogen intermediate adsorption. Moreover, Ru sites also serve as active centers for the stepwise dehydrogenation of hydrazine during HzOR.

3.2.5 Other catalysts. Beyond the well-studied transition metal catalysts, alternative materials such as Cu-based and Mn-based catalysts have been investigated for their potential in bifunctional HzOR and HER catalysis. Sun's group highlighted a Cu_3P nanoarray anchored on copper foam (Cu_3P/CF), which serves as a highly efficient electrocatalyst for hydrazine-assisted overall water splitting.[78] This configuration, employing Cu_3P/CF as the anode for HzOR and concurrently as the cathode for HER, manages to reach a current density of 100 mA cm^{-2} at an applied voltage of 0.72 V in a 1 M KOH solution containing 0.5 M hydrazine, while also demonstrating robust long-term stability. In another development, Liu *et al.* unveiled an innovative catalyst constituted of single atomic Mn sites embedded within a boron–nitrogen co-doped carbon matrix (referred to as Mn–SA/BNC).[79] This catalyst manifests extraordinary bifunctional reactivity, characterized by a low HER potential of −51 mV and an HzOR potential of 132 mV at a current density of 10 mA cm^{-2}. Deployed within a two-electrode setup for overall hydrazine splitting, Mn–SA/BNC necessitates a mere cell voltage of 0.41 V to yield a current density of 10 mA cm^{-2}, coupled with remarkable durability and near-perfect faradaic efficiency for hydrogen synthesis. These outcomes accentuate the viability of Mn–SA/BNC as a potent and stable catalyst for sustainable hydrogen generation through the pathway of hydrazine splitting.

3.3 Ammonia

The AmOR has emerged as a viable alternative to the OER in HWE systems, offering lower oxidation potentials (−0.77 V) compared to water oxidation, suggesting a potential pathway for energy conversion *via* electrolysis.[80,81] Ammonia-containing wastewater, often a byproduct of industrial processes, poses significant treatment challenges that can lead to the eutrophication of water bodies and adversely impact aquatic ecosystems.[82] By integrating AmOR with the HER, these hybrid systems not only enhance the energy efficiency of hydrogen generation but also provide an environmentally friendly solution to wastewater treatment. In ammonia-assisted water

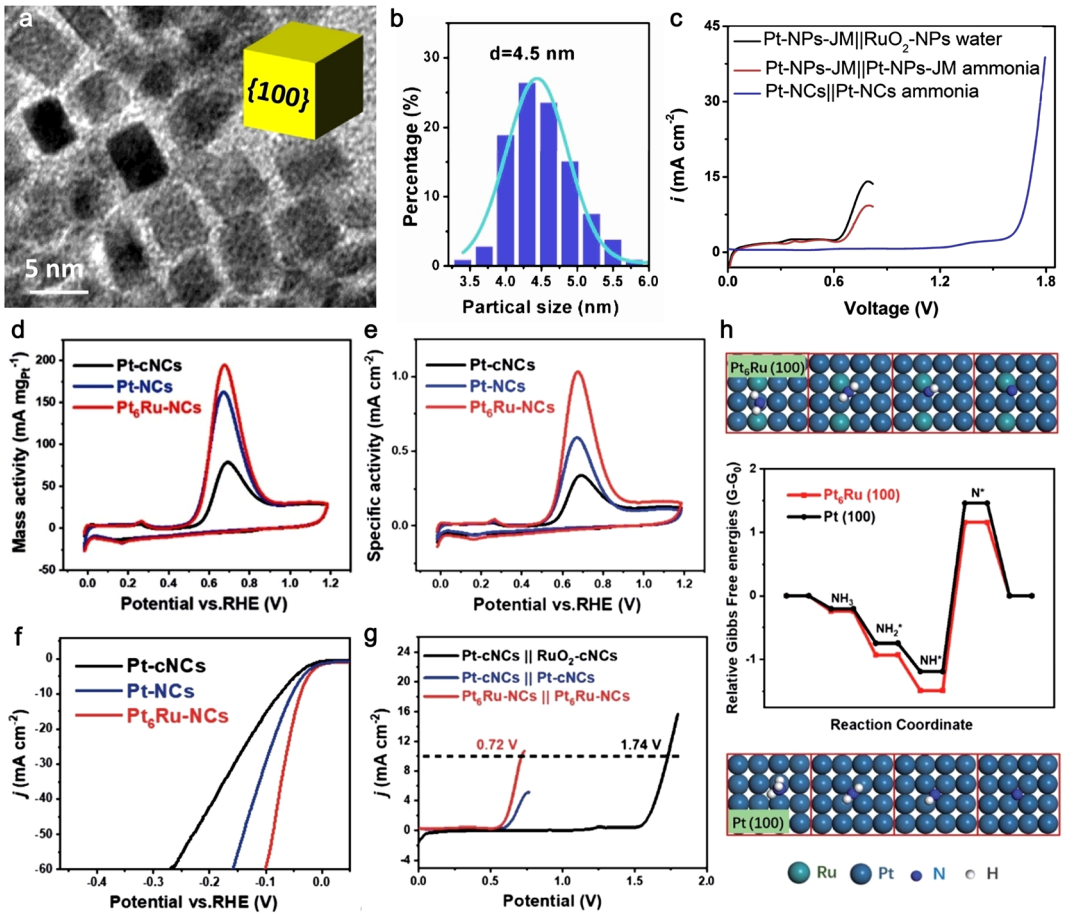

Fig. 8 (a) TEM image and (b) size distribution of Pt–NCs. (c) LSV curves of Pt–NPs-JM and comparison sample in ammonia electrolyzer.[80] Copyright 2020, Elsevier. (d) Mass and (e) specific activities of the AmOR for Pt_6Ru–NCs and comparison samples. (f) HER polarization curves and (g) ammonia-assisted water electrolysis of Pt_6Ru–NCs and comparison samples. (h) Gibbs free energy changes of AmOR on Pt_6Ru (100) and Pt (100) planes.[83] Copyright 2021, Royal Society of Chemistry.

splitting, aside from the cathodic HER, the anodic reaction can be represented as follows:

$$\text{Anode reaction: } 2NH_3 + 6OH^- \rightarrow N_2 + 6H_2O + 6e^- \quad (7)$$

3.3.1 Pt-based catalysts. Pt continues to reign as the premier electrocatalyst for the ammonia electro-oxidation reaction in alkaline environments. Concurrently, Pt stands out as the most active and durable electrocatalyst for alkaline HER. Despite its efficacy, the prohibitive cost and limited availability of Pt metal impede its broad implementation across various electrocatalytic energy conversion technologies. Consequently, optimizing Pt utilization and enhancing its electrocatalytic performance emerge as critical imperatives. Considering the structure-sensitive nature of both AmOR and HER, modulating morphology and surface crystalline orientation presents a potent avenue for boosting electroactivity. Chen's group reported the fabrication of high-quality Pt nanocubes (Pt–NCs), measuring 4.5 nm in size, through a straightforward hydrothermal synthesis approach (Fig. 8(a) and (b)).[80] These Pt–NCs exhibited exceptional electroactivity for AmOR and HER in alkaline media. A symmetric ammonia electrolyzer, leveraging these bifunctional Pt–NCs, operated at a mere 0.68 V for hydrogen generation, significantly lower than that of water electrolysis (approximately 1.8 V) (Fig. 8(c)).

Building on this foundation, the team further developed high-quality Pt_xRu nanocubes (Pt_xRu–NCs) with tunable compositions and exposed (100) facets by a polyallylamine-assisted hydrothermal technique.[83] For AmOR, Pt_6Ru–NCs outperformed other Pt_xRu–NCs, Pt–NCs, and commercial Pt nanocrystals, with a significantly higher mass activity (192 mA mg_{Pt}^{-1}) and specific activity (1.02 mA cm^{-2}) (Fig. 8(d) and (e)). DFT computations illuminated that the Pt_6Ru (100) plane offers a more energetically advantageous site for AmOR than the Pt (100) plane, attributed to enhanced binding affinities for $*NH_2$ and *NH intermediates (Fig. 8(h)). Regarding HER, the optimized Pt_6Ru–NCs exhibited the lowest overpotential (37.6 mV) at a current density of 10 mA cm^{-2} (Fig. 8(f)). The superior bifunctional activity of Pt_6Ru–NCs in AmOR and HER is ascribed to synergistic effects between crystal surface properties and Pt–Ru bimetallic interactions. A symmetrical ammonia electrolyzer was assembled, demanding only 0.72 V for hydrogen

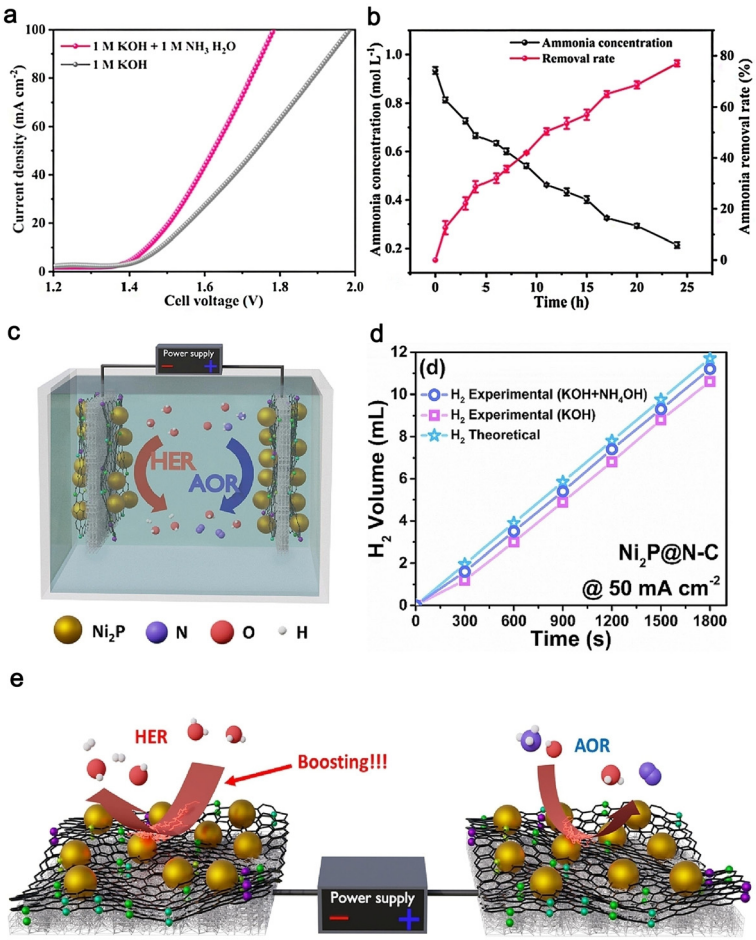

Fig. 9 (a) LSV curves of B–NiFe-LDH/NF for water electrolysis and ammonia-assisted water electrolysis. (b) Ammonia concentration and removal rate of 1 M KOH + 1 M $NH_3{\cdot}H_2O$ electrolyzed for 24 h.[86] Copyright 2023, Elsevier. (c) Diagram of an ammonia-assisted water electrolyzer using Ni_2P@N–C as both anode and cathode. (d) Theoretical and measured H_2 production of Ni_2P@N–C in KOH solution with and without $NH_3{\cdot}H_2O$. (e) Schematic of the AmOR and HER reaction processes.[87] Copyright 2023, Elsevier.

production, thus exemplifying an energy-efficient strategy for hydrogen synthesis (Fig. 8(g)).

3.3.2 Ni-based catalysts. The exorbitant costs associated with noble-metal catalysts have catalyzed the quest for transition-metal alternatives capable of bifunctional operations in ammonia abatement and hydrogen synthesis. Nickel-based catalysts have surfaced as notably viable options, exhibiting remarkable proficiency in both the AmOR and the HER.[84,85] A significant stride in this domain was documented by Wang and colleagues, who adeptly employed B–NiFe-LDH/NF electrodes to expedite the anodic oxidation of ammonia, effectively supplanting the comparatively sluggish OER.[86] Linear sweep voltammetry (LSV) curves, depicted in Fig. 9(a), unveiled exceptional performance, with a current density of 100 mA cm^{-2} attained at a cell voltage of 1.781 V, a significant 202 mV reduction relative to the potential required for conventional water electrolysis. This ammonia-assisted water electrolysis not only yielded a superior hydrogen output compared to standard water electrolysis but also realized an average Faraday efficiency nearing 100%. Furthermore, the average energy consumption per liter of hydrogen generation (0.003951 kW h L^{-1}) was roughly 1.547 times less than that of an ammonia-free KOH solution (0.006112 kW h L^{-1}). During constant current electrolysis in simulated ammonia-containing wastewater, the ammonia concentration in the electrolyte dwindled to 0.214 mol L^{-1} as the reaction progressed, achieving a removal efficacy of 78.6% post 24 hours of operation (Fig. 9(b)). Typically, ammonia oxidation not only eradicates NH_4^+ from the electrolyte but also generates by-products such as NO_2^- and NO_3^-. Significantly, no NO or N_2O gases were detected in this setup. At the end of the reaction, the NO_2^- concentration peaked at 0.093 mol L^{-1}, while the NO_3^- concentration steadily rose to 0.174 mol L^{-1}. These findings suggest that the B–NiFe-LDH/NF electrode holds promise as a robust bifunctional electrocatalyst for efficient ammonia elimination and energy-saving hydrogen production in practical applications.

Furthermore, Ni_2P nanoparticles supported on N-doped carbon (Ni_2P@N–C) were developed, exhibiting a significantly higher anodic current density of 47.4 mA cm^{-2} compared to that of Ni_2P (16.0 mA cm^{-2}) at 1.6 V.[87] The enhanced electrical conductivity and charge kinetics, attributed to the formation of N-doped carbon on the surface of Ni_2P nanoparticles, led to improved ammonia removal efficiency, with a 78% reduction in ammonia concentration relative to its initial level. The volume of H_2 generated *via* AmOR reached 11.2 mL within 30 minutes, outperforming the output from traditional water electrolysis (Fig. 9(c)–(e)).

3.3.3 Multitransition-metal catalysts. To overcome the inherent scaling relationships between various intermediates involved in ammonia electrolysis, several effective multi-transition-metal catalysts have been developed. Perovskite oxides, delineated by the generic formula ABO_3, are ascending as a new category of superior electrocatalysts for multiple catalytic reactions, owing to their flexible compositions and adjustable electronic structures.[85] Notably, the B-site is amenable to occupation by most transition metal ions. Substitution at the B-site increases surface defects and modulates the oxidation states of the B-site cations, thereby enhancing activation for

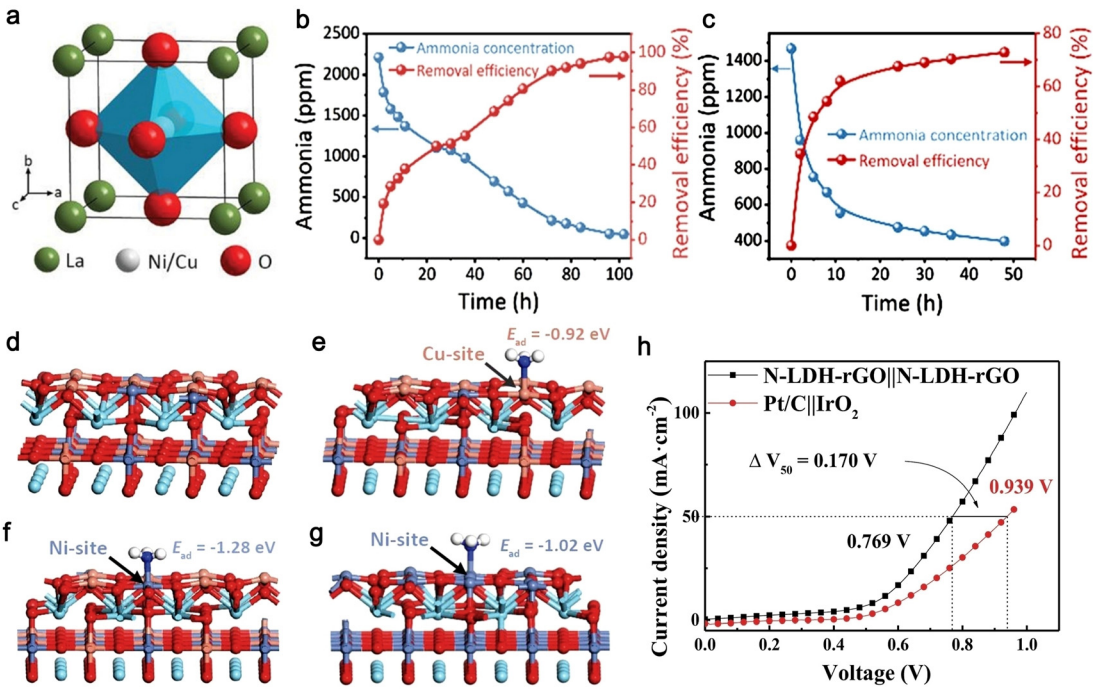

Fig. 10 (a) Perovskite structure. Concentration profile of ammonia and removal efficiency of LNCO55–Ar in (b) 0.5 M KOH containing 2210 ppm NH_4Cl and (c) real wastewater with 0.5 M KOH. (d) The calculation model of $LaNi_{0.5}Cu_{0.5}O_{3-\delta}$. (e)–(g) Configuration diagram of ammonia molecule adsorbed on different sites.[85] Copyright 2021, Wiley-VCH. (h) LSV curves of N–NiZnCu LDH/rGO and commercial Pt/C||IrO_2.[84] Copyright 2020, Elsevier.

Table 1 Performance comparison of bifunctional transition-metal catalysts for hydrogen production from nitrogenous wastewater

Catalysts	Additives in 1 M KOH	E_{10} for HER (V)	E_{10} for NmOR (V)	E_{cell} in HWE (V)	E_{cell} in OWE (V)	Electricity consumption (kW h Nm^{-3} H_2)	Electricity consumption saving (%)	Ref.
$Co_xCu_{2-x}Se$/CF	0.33 M urea	−0.15	1.35	1.51@10 mA cm^{-2}	1.64@10 mA cm^{-2}	3.61	7.9	88
NiS/MoS_2@FCP	0.4 M urea	−0.128	~1.42	1.42@10 mA cm^{-2}	1.72@10 mA cm^{-2}	3.38	17.4	89
$Cu_{0.5}Ni_{0.5}$/NF	0.5 M urea	−0.028	1.33	1.38@10 mA cm^{-2}	1.63@10 mA cm^{-2}	3.30	15.3	90
O–NiMoP/NF	0.5 M urea	−0.054	~1.31	1.36@10 mA cm^{-2}	1.58@10 mA cm^{-2}	3.25	13.9	91
Ni_9Fe_1-LDHs	0.5 M urea	−0.07	~1.35	~1.42@10 mA cm^{-2}	1.6@10 mA cm^{-2}	3.39	11.3	92
Ni_2P/MoO_2/NF	0.5 M urea	−0.034	1.35	1.35@10 mA cm^{-2}	1.46@10 mA cm^{-2}	3.22	7.5	93
$NiSe_2$/$MoSe_2$	0.5 M urea	−0.079	1.34	1.63@100 mA cm^{-2}	1.91@100 mA cm^{-2}	3.91	14.6	94
Ni_3Se_4–$MoSe_2$/Co@C	0.5 M urea	−0.034	1.311	1.51@100 mA cm^{-2}	1.73@100 mA cm^{-2}	3.61	12.7	95
Fe–$Co_{0.85}Se$/FeCo LDH	0.5 M urea	−0.037	1.29	1.52@100 mA cm^{-2}	1.64@100 mA cm^{-2}	3.63	7.3	96
Mo–NiS	0.5 M urea	−0.174	~1.33	1.57@200 mA cm^{-2}	1.83@200 mA cm^{-2}	3.75	14.7	27
NiCoO–MoO_x/NC	0.5 M urea	−0.045	1.28	1.7@250 mA cm^{-2}	1.9@250 mA cm^{-2}	4.06	10.6	97
Ni_3S_2–$NiMoO_4$/NF	0.5 M urea	−0.263	1.30	1.73@1 A cm^{-2}	2.06@1 A cm^{-2}	4.13	16.0	98
6W–O–CoP/NF	0.1 M N_2H_4	−0.072	−0.051	0.009@10 mA cm^{-2}	1.62@10 mA cm^{-2}	0.02	99.5	99
N–Ni_5P_4@CoP/CFP	0.1 M N_2H_4	−0.056	−0.032	0.037@10 mA cm^{-2}	0.322@10 mA cm^{-2}	0.09	88.5	100
W@Co_2P/NF	0.1 M N_2H_4	−0.075	−0.08	0.18@100 mA cm^{-2}	1.73@100 mA cm^{-2}	0.43	89.6	101
Ni_2P/Zn–Ni–P	0.1 M N_2H_4	−0.063	0.027	0.36@100 mA cm^{-2}	1.94@100 mA cm^{-2}	0.86	81.6	102
FeCoP/NF	0.2 M N_2H_4	−0.01	0.203	0.21@200 mA cm^{-2}	1.81@200 mA cm^{-2}	0.57	87.0	103
Mo_2C@C/Co@C	0.2 M N_2H_4	−0.071	−0.083	0.49@300 mA cm^{-2}	~2.2@300 mA cm^{-2}	1.17	77.7	104
CoFeNiCrMnP/NF	0.4 M N_2H_4	−0.01	−0.085	0.14@200 mA cm^{-2}	1.68@200 mA cm^{-2}	0.33	91.7	105
$(P–Co/Ni_3P)_{A3}$/NF	0.4 M N_2H_4	−0.01	−0.079	0.05@300 mA cm^{-2}	1.82@300 mA cm^{-2}	0.12	97.3	106
$Ni_{1.4}Mn_{0.6}P$ NCs	0.5 M N_2H_4	−0.1	0.055	0.059@10 mA cm^{-2}	1.45@10 mA cm^{-2}	0.14	95.9	107
Ni_2P@N–C	0.5 M $NH_3·H_2O$	−0.161	~1.4	1.57@50 mA cm^{-2}	~1.72@50 mA cm^{-2}	3.75	8.7	87
B–NiFe-LDH/NF	1 M $NH_3·H_2O$	−0.097	~1.35	1.78@100 mA cm^{-2}	1.98@100 mA cm^{-2}	4.26	10.2	86
CoS@NiCu	2000 ppm $NH_3·H_2O$	−0.1	~1.38	1.5@100 mA cm^{-2}	1.65@100 mA cm^{-2}	3.59	9.1	108

various catalytic reactions. Leveraging these advantages, Tao's group synthesized a perovskite $LaNi_{0.5}Cu_{0.5}O_{3-\delta}$ annealed in argon (LNCO55–Ar), wherein the B-site is occupied by Ni and Cu (Fig. 10(a)).[85] Intriguingly, LNCO55–Ar emerged as not only a paragon catalyst for AmOR but also a superior catalyst for HER under alkaline circumstances. Benefiting from its transcendent catalytic activity, the symmetric ammonia electrolyzer based on LNCO55–Ar exhibited a superb ammonia removal efficiency of ≈100% in a 2210 ppm ammonia solution after applying 1.23 V for 100 hours at room temperature (Fig. 10(b)). When applied to real ammonia-containing wastewater, a removal efficiency of ammonia in excess of 70% was attained post 48 hours (Fig. 10(c)). Combined experimental results and DFT calculations disclosed that the electrocatalytic activity for AmOR and HER was primarily ascribable to the increased active sites from morphological evolution during electrochemical reactions, the introduction of oxygen vacancies, and the synergistic effect of B-site cations (Fig. 10(d)–(g)).

Furthermore, transition metal-based LDHs, especially ternary LDHs that incorporate an additional metal species, hold the potential to deliver higher catalytic activities. A bifunctional catalyst comprising N-doped NiZnCu-layered double hydroxides coupled with reduced graphene oxide on NF (N–NiZnCu LDH/rGO) was fabricated through a straightforward hydrothermal and calcination methodology.[84] The distinctive morphology of N–NiZnCu LDH/rGO exposed a large number of active sites for hybrid water electrolysis. Experiments showed that at a current density of 10 mA cm^{-2}, the voltages for AmOR, UOR, and HzOR were 0.489 V, 1.305 V, and 0.010 V, respectively, with commendable stability (exceeding 3000 CV cycles), markedly surpassing the benchmarks of Pt/C||IrO_2 (Fig. 10(h)). This study demonstrates that N–NiZnCu LDH/rGO can replace precious metals for commercial hydrogen energy production in hybrid water electrolysis. A comprehensive comparison of the performance of various bifunctional transition metal catalysts for hydrogen production in nitrogen-containing wastewater is presented in Table 1.

4. Conclusions and perspectives

This review systematically presents the development status of bifunctional transition-metal catalysts for energy-saving hydrogen production from nitrogenous wastewater, including urea, hydrazine, and ammonia, highlighting their potential to simultaneously address the degradation of organic nitrogen-containing pollutants and hydrogen energy generation. The fundamental principles of each hybrid water electrolysis system were thoroughly introduced. Subsequently, the recent advances in bifunctional transition-metal catalysts and their catalytic mechanisms were overviewed. Finally, it provides a detailed summary and comparison of representative bifunctional catalysts, with a particular emphasis on electricity consumption and energy-saving efficiency. The integration of bifunctional catalysts not only reduces the costs associated with water splitting systems but also simplifies the overall process, enhancing its economic feasibility and sustainability.

Looking ahead, as energy-saving hydrogen production technology progresses and costs fall, hydrogen generation from nitrogenous wastewater may become a viable option for the

energy economy. However, existing hybrid water electrolysis systems face several challenges, including catalyst design and large-scale implementation.

(1) The development of efficient, stable, and cost-effective electrocatalysts is a fundamental objective in the field of hydrogen production from nitrogenous wastewater. Traditional methods, including trial-and-error experiments and theoretical calculations, are both time-consuming and resource-intensive, thereby hindering the pace of catalyst development. In contrast, the rapid advancement of machine learning (ML) has introduced a transformative paradigm for catalyst discovery, offering efficient and precise methodologies for material screening and optimization of synthesis conditions. ML models can predict material properties and swiftly screen potential electrocatalysts within the existing material space. These predictions can subsequently be validated through experimental or computational methods, significantly reducing the reliance on trial-and-error approaches and minimizing associated costs. Moreover, ML provides valuable insights for optimizing existing catalysts and guiding the synthesis of novel materials. Despite its promising potential, ML has not yet fully revolutionized the field of electrocatalysis. This is primarily due to the absence of systematic and standardized data-driven approaches, which are essential for accelerating scientific discovery. However, as these challenges are addressed and standardized systems are established, ML is poised to make a substantial impact on research related to hydrogen generation from nitrogenous wastewater.

(2) The lack of advanced *in situ* characterization techniques hampers a deeper understanding of reaction mechanisms. Anodic reactions in these systems often involve complex electron transfer processes and multiple intermediate adsorption states, making it challenging to definitively identify the types of intermediates and their adsorption forms. While current approaches primarily rely on *in situ* Raman spectroscopy combined with DFT calculations, the development of new *in situ* techniques is urgently needed. Future efforts should integrate *in situ* surface-enhanced Raman spectroscopy (SERS) and *in situ* electrochemical impedance spectroscopy (EIS) to identify active species, and utilize *in situ* Fourier-transform infrared (FTIR) spectroscopy to validate dissociation pathways and products. These advancements will lay the groundwork for a comprehensive understanding of structure–activity–selectivity relationships, ultimately facilitating the design, detection, and identification of more efficient catalysts.

(3) Research on bifunctional transition-metal catalysts for hydrogen generation from nitrogenous wastewater in large-scale electrolyzers, such as alkaline electrolysis cells and anion exchange membrane (AEM) systems, has been relatively neglected. However, expanding research into these large-scale devices is essential for practical applications. In real-world scenarios, the concentration of contaminants in wastewater is significantly lower than in laboratory conditions. This lower concentration results in reduced current densities, necessitating the concurrent oxidation of nitrogen compounds alongside water oxidation to sustain the electrolysis process. This concomitant oxidation is unavoidable. Furthermore, as electrolysis progresses, the concentration of contaminants decreases, leading to an increase in the overall cell voltage and, consequently, higher total energy consumption. These challenges must be addressed to make large-scale electrolyzers viable for practical use.

(4) Nitrogenous wastewater is usually more complicated in industrial applications, comprising a variety of contaminants that present significant hurdles to catalyst activity, stability, and selectivity. It is essential to conduct evaluations in actual wastewater in order to effectively improve the application ability of catalysts.

Despite the aforementioned challenges and issues, bifunctional transition-metal electrocatalysts remain a prospective avenue for the commercial feasibility of various NWE systems, since they provide efficient H_2 generation and wastewater treatment. This novel approach is intended to successfully solve the limitations of conventional water electrolysis. This review is considered to give crucial insights for improving NWE technology, which will aid in the development of energy-saving hydrogen production.

Author contributions

Yue Zhou: investigation, conceptualization, writing – original draft, editing, visualisation, and funding acquisition. Liang Zhang: writing – original draft, editing, and visualisation. Xin Yang: writing – review and editing, and visualisation. Guiyue Xu: writing – review and editing, and visualisation. Chao Meng: writing – review and editing, and visualisation. Guoqiang Li: writing – review and editing. Yan Lin: writing – review and editing. Chongzheng Sun: writing – review and editing. Ning Zhang: writing – review and editing. Ran Yi: writing – review and editing, supervision. Kun Zhang: writing – review and editing, funding acquisition, and supervision. Lichao Jia: conceptualization, writing – review and editing, funding acquisition, and supervision.

Data availability

No primary research results, software or code have been included and no new data were generated or analysed as part of this review.

Conflicts of interest

There are no conflicts to declare.

Acknowledgements

This work was supported by the National Defense Science and Technology Innovation Project, the National Natural Science Foundation of China (no. 52301279, 52304067 and 51901115), Outstanding Youth Innovation Team of Universities in Shandong Province (2024KJH067), the Shandong Provincial Natural Science Foundation, China (ZR2023MB122, ZR2023QB117, and

ZR2024QB031), the Key Research Project of Jining City (2023KJHZ009), and Innovation Fund Project for Graduate Students of China University of Petroleum (East China) supported by the Fundamental Research Funds for the Central Universities (no. 23CX04010A).

References

1 C. J. Chen, H. Y. Jin, P. T. Wang, X. G. Sun, M. Jaroniec, Y. Zheng and S. Z. Qiao, *Chem. Soc. Rev.*, 2024, **53**, 2022–2055.
2 E. B. Agyekum, C. Nutakor, A. M. Agwa and S. Kamel, *Membranes*, 2022, **12**, 173.
3 H. Wu, Q. X. Huang, Y. Y. Shi, J. W. Chang and S. Y. Lu, *Nano Res.*, 2023, **16**, 9142–9157.
4 J. T. Ren, L. Chen, H. Y. Wang and Z. Y. Yuan, *Chem. Soc. Rev.*, 2023, **52**, 8319–8373.
5 W. Z. Zhang, M. H. Liu, X. Gu, Y. X. Shi, Z. F. Deng and N. S. Cai, *Chem. Rev.*, 2023, **123**, 7119–7192.
6 P. Xue, M. Qiao, J. Miao, Y. Tang, D. Zhu and C. Guo, *Chem. Commun.*, 2024, **60**, 6423–6426.
7 A. H. Al-Naggar, N. M. Shinde, J. S. Kim and R. S. Mane, *Coord. Chem. Rev.*, 2023, **474**, 214864.
8 Y. J. Lee and S.-K. Park, *Rare Met.*, 2024, **43**, 522–532.
9 J. T. Ren, L. Chen, H. Y. Wang, W. W. Tian and Z. Y. Yuan, *Energy Environ. Sci.*, 2024, **17**, 49–113.
10 X. B. Liu, J. Q. Chi, H. M. Mao and L. Wang, *Adv. Energy Mater.*, 2023, **13**, 202301438.
11 R. Wan, T. Yuan, L. Wang, B. Li, M. Liu and B. Zhao, *Nat. Catal.*, 2024, **7**, 1288–1304.
12 D. Kong, C. Meng, Y. Wang, X. Chen, J. Zhang, L. Zhao, J. Ji, L. Zhang and Y. Zhou, *Appl. Catal., B*, 2024, **343**, 123578.
13 G. Yang, T. Yang, Z. Wang, K. Wang, M. Zhang, P. D. Lund and S. Yun, *Adv. Powder Mater.*, 2024, **3**, 100224.
14 M. J. Sun, R. Y. Ge, S. Li, L. M. Dai, Y. R. Li, B. Liu and W. X. Li, *J. Energy Chem.*, 2024, **91**, 453–474.
15 H. Wang, T. T. Zhai, Y. F. Wu, T. Zhou, B. B. Zhou, C. X. Shang and Z. X. Guo, *Adv. Sci.*, 2023, **10**, 202301706.
16 X. Han, L. Shi, H. Chen and X. Zou, *Chem. Commun.*, 2024, **60**, 3453–3456.
17 K. Veeramani, G. Janani, J. Kim, S. Surendran, J. Lim, S. C. Jesudass, S. Mahadik, H. Y. J. Lee, T. H. Kim, J. K. Kim and U. Sim, *Renewable Sustainable Energy Rev.*, 2023, **177**, 113227.
18 Q. Z. Qian, Y. Zhu, N. Ahmad, Y. F. Feng, H. K. Zhang, M. Y. Cheng, H. H. Liu, C. Xiao, G. Q. Zhang and Y. Xie, *Adv. Mater.*, 2024, **36**, 202306108.
19 X. Y. Peng, L. B. Zeng, D. S. Wang, Z. B. Liu, Y. Li, Z. J. Li, B. Yang, L. C. Lei, L. M. Dai and Y. Hou, *Chem. Soc. Rev.*, 2023, **52**, 2193–2237.
20 P. Y. Jiang, T. S. Zhou, J. Bai, Y. Zhang, J. H. Li, C. H. Zhou and B. X. Zhou, *Water Res.*, 2023, **235**, 119914.
21 Y. J. Qin, K. C. Wang, Q. Xia, S. Q. Yu, M. A. Zhang, Y. An, X. D. Zhao and Z. Zhou, *Chem. Eng. J.*, 2023, **451**, 138789.
22 T. Z. Wang, L. C. Miao, S. Y. Zheng, H. Y. Qin, X. J. Cao, L. Yang and L. F. Jiao, *ACS Catal.*, 2023, **13**, 4091–4100.
23 Y. Zhu, K. Fan, C. S. Hsu, G. Chen, C. Chen, T. Liu, Z. Lin, S. She, L. Li, H. Zhou, Y. Zhu, H. M. Chen and H. Huang, *Adv. Mater.*, 2023, **35**, 2301133.
24 F. Vitse, M. Cooper and G. G. Botte, *J. Power Sources*, 2005, **142**, 18–26.
25 L. Quan, H. Jiang, G. L. Mei, Y. J. Sun and B. You, *Chem. Rev.*, 2024, **124**, 3694–3812.
26 X. X. Wang, J. M. Wang, X. P. Sun, S. Wei, L. Cui, W. R. Yang and J. Q. Liu, *Nano Res.*, 2018, **11**, 988–996.
27 B. Sang, C. Xue, S. Guo, X. Wng, S. Xie, C. Wang and R.-Q. Li, *Chem. Commun.*, 2024, **60**, 6643–6646.
28 P. Wang, J. Zheng, X. Xu, Y.-Q. Zhang, Q.-F. Shi, Y. Wan, S. Ramakrishna, J. Zhang, L. Zhu, T. Yokoshima, Y. Yamauchi and Y.-Z. Long, *Adv. Mater.*, 2024, **36**, 2404806.
29 Y. Zhou, Y. Wang, D. Kong, Q. Zhao, L. Zhao, J. Zhang, X. Chen, Y. Li, Y. Xu and C. Meng, *Adv. Funct. Mater.*, 2023, **33**, 2210656.
30 L.-L. Zhang, W. Li, M. Yin, C. Cui, W. Ma and Z. Zhou, *ACS Sustainable Chem. Eng.*, 2024, **12**, 17263–17271.
31 X. Gao, S. Zhang, P. Wang, M. Jaroniec, Y. Zheng and S.-Z. Qiao, *Chem. Soc. Rev.*, 2024, **53**, 1552–1591.
32 G. Zhan, L. Hu, H. Li, J. Dai, L. Zhao, Q. Zheng, X. Zou, Y. Shi, J. Wang, W. Hou, Y. Yao and L. Zhang, *Nat. Commun.*, 2024, **15**, 5918.
33 Q. Zhao, C. Meng, D. Kong, Y. Wang, H. Hu, X. Chen, Y. Han, X. Chen, Y. Zhou, M. Lin and M. Wu, *ACS Sustainable Chem. Eng.*, 2021, **9**, 15582–15590.
34 S. K. Dong, M. A. Page, N. Massalha, A. Hur, K. Hur, K. Bokenkamp, E. D. Wagner and M. J. Plewa, *Environ. Sci. Technol.*, 2019, **53**, 9139–9147.
35 S. R. Feng, H. H. Ngo, W. S. Guo, S. W. Chang, D. D. Nguyen, D. L. Cheng, S. Varjani, Z. F. Lei and Y. Liu, *Bioresour. Technol.*, 2021, **335**, 125278.
36 P. Dange, S. Pandit, D. Jadhav, P. Shanmugam, P. K. Gupta, S. Kumar, M. Kumar, Y. H. Yang and S. K. Bhatia, *Sustainability*, 2021, **13**, 8796.
37 V. G. Gude, *J. Cleaner Prod.*, 2016, **122**, 287–307.
38 J. X. Li, S. L. Wang, S. J. Sun, X. Wu, B. G. Zhang and L. G. Feng, *J. Mater. Chem. A*, 2022, **10**, 9308–9326.
39 W. Chen, L. T. Xu, X. R. Zhu, Y. C. Huang, W. Zhou, D. D. Wang, Y. Y. Zhou, S. Q. Du, Q. L. Li, C. Xie, L. Tao, C. L. Dong, J. L. Liu, Y. Y. Wang, R. Chen, H. Su, C. Chen, Y. Q. Zou, Y. F. Li, Q. H. Liu and S. Y. Wang, *Angew. Chem., Int. Ed.*, 2021, **60**, 7297–7307.
40 D. N. Liu, T. T. Liu, L. X. Zhang, F. L. Qu, G. Du, A. M. Asiri and X. P. Sun, *J. Mater. Chem. A*, 2017, **5**, 3208–3213.
41 E. T. Sayed, T. Eisa, H. O. Mohamed, M. A. Abdelkareem, A. Allagui, H. Alawadhi and K. J. Chae, *J. Power Sources*, 2019, **417**, 159–175.
42 B. Zhu, Z. Liang and R. Zou, *Small*, 2020, **16**, 1906133.
43 R. P. Forslund, C. T. Alexander, A. M. Abakumov, K. P. Johnston and K. J. Stevenson, *ACS Catal.*, 2019, **9**, 2664–2673.
44 J. Li, J. Li, T. Liu, L. Chen, Y. Li, H. Wang, X. Chen, M. Gong, Z.-P. Liu and X. Yang, *Angew. Chem., Int. Ed.*, 2021, **60**, 26656–26662.
45 N. Chen, Y.-X. Du, G. Zhang, W.-T. Lu and F.-F. Cao, *Nano Energy*, 2021, **81**, 105605.
46 D. Li, W. Wan, Z. Wang, H. Wu, S. Wu, T. Jiang, G. Cai, C. Jiang and F. Ren, *Adv. Energy Mater.*, 2022, **12**, 2201913.
47 Q. Zhang, F. M. D. Kazim, S. Ma, K. Qu, M. Li, Y. Wang, H. Hu, W. Cai and Z. Yang, *Appl. Catal., B*, 2021, **280**, 119436.
48 Z. Shi, Y. Zhang, W. Guo, Z. Niu, Y. Chen and J. Huang, *Adv. Funct. Mater.*, 2025, **35**, 2414935.
49 X. Xu, H. Ullah, M. Humayun, L. Li, X. Zhang, M. Bououdina, D. P. Debecker, K. Huo, D. Wang and C. Wang, *Adv. Funct. Mater.*, 2023, **33**, 2303986.
50 M. Liu, W. Zou, S. Qiu, N. Su, J. Cong and L. Hou, *Adv. Funct. Mater.*, 2024, **34**, 2310155.
51 Y. Jiang, S. Gao, G. Xu and X. Song, *J. Mater. Chem. A*, 2021, **9**, 5664–5674.
52 Z. Ji, Y. Song, S. Zhao, Y. Li, J. Liu and W. Hu, *ACS Catal.*, 2022, **12**, 569–579.
53 M. Pan, G. Qian, T. Yu, J. Chen, L. Luo, Y. Zou and S. Yin, *Chem. Eng. J.*, 2022, **435**, 134986.
54 Z. Liu, Z. Lu, Y. Cao, J. Xie, J. Hu and A. Hao, *Inorg. Chem.*, 2024, **63**, 2803–2813.
55 X. F. Lu, S. L. Zhang, W. L. Sim, S. Gao and X. W. Lou, *Angew. Chem., Int. Ed.*, 2021, **60**, 22885–22891.
56 H. Xi, X. Yang, W. Guo, H. Pang, X. Leng, X. Huang and F. Meng, *J. Colloid Interface Sci.*, 2025, **683**, 860–869.
57 S. Wang, A. Hao and Z. Liu, *ACS Appl. Nano Mater.*, 2024, **7**, 28602–28611.
58 J.-Y. Zhang, H. Wang, Y. Tian, Y. Yan, Q. Xue, T. He, H. Liu, C. Wang, Y. Chen and B. Y. Xia, *Angew. Chem., Int. Ed.*, 2018, **57**, 7649–7653.
59 D. R. Cummins, U. Martinez, A. Sherehiy, R. Kappera, A. Martinez-Garcia, R. K. Schulze, J. Jasinski, J. Zhang, R. K. Gupta, J. Lou, M. Chhowalla, G. Sumanasekera, A. D. Mohite, M. K. Sunkara and G. Gupta, *Nat. Commun.*, 2016, **7**, 11857.
60 F. Luo, S. Pan, Y. Xie, C. Li, Y. Yu, H. Bao and Z. Yang, *Adv. Sci.*, 2023, **10**, 2305058.
61 H.-L. Huang, X. Guan, H. Li, R. Li, R. Li, S. Zeng, S. Tao, Q. Yao, H. Chen and K. Qu, *Chem. Commun.*, 2022, **58**, 2347–2350.

62 Y. Zhu, J. Zhang, Q. Qian, Y. Li, Z. Li, Y. Liu, C. Xiao, G. Zhang and Y. Xie, *Angew. Chem., Int. Ed.*, 2022, **61**, e202113082.
63 Z. Wang, L. Xu, F. Huang, L. Qu, J. Li, K. A. Owusu, Z. Liu, Z. Lin, B. Xiang, X. Liu, K. Zhao, X. Liao, W. Yang, Y.-B. Cheng and L. Mai, *Adv. Energy Mater.*, 2019, **9**, 1900390.
64 Y. Li, J. Li, Q. Qian, X. Jin, Y. Liu, Z. Li, Y. Zhu, Y. Guo and G. Zhang, *Small*, 2021, **17**, 2008148.
65 H.-M. Yang, H.-Y. Wang, M.-L. Sun and Z.-Y. Yuan, *Chem. Eng. J.*, 2023, **475**, 146134.
66 H.-Y. Wang, L. Wang, J.-T. Ren, W.-W. Tian, M.-L. Sun and Z.-Y. Yuan, *Nano-Micro Lett.*, 2023, **15**, 155.
67 Q. Sun, Y. Li, J. Wang, B. Cao, Y. Yu, C. Zhou, G. Zhang, Z. Wang and C. Zhao, *J. Mater. Chem. A*, 2020, **8**, 21084–21093.
68 C. Deng, C. Y. Toe, X. Li, J. Tan, H. Yang, Q. Hu and C. He, *Adv. Energy Mater.*, 2022, **12**, 2201047.
69 Y. Liu, J. Zhang, Y. Li, Q. Qian, Z. Li, Y. Zhu and G. Zhang, *Nat. Commun.*, 2020, **11**, 1853.
70 X. Wei, S. Zhang, X. Lv, S. Dai, H. Wang and M. Huang, *Appl. Catal., B*, 2024, **345**, 123661.
71 X. Liu, J. He, S. Zhao, Y. Liu, Z. Zhao, J. Luo, G. Hu, X. Sun and Y. Ding, *Nat. Commun.*, 2018, **9**, 4365.
72 Q. Xue, H. Huang, J.-Y. Zhu, Y. Zhao, F.-M. Li, P. Chen and Y. Chen, *Appl. Catal., B*, 2020, **278**, 119269.
73 N. Jia, Y. Liu, L. Wang, P. Chen, X. Chen, Z. An and Y. Chen, *ACS Appl. Mater. Interfaces*, 2019, **11**, 35039–35049.
74 J. Yang, L. Xu, W. Zhu, M. Xie, F. Liao, T. Cheng, Z. Kang and M. Shao, *J. Mater. Chem. A*, 2022, **10**, 1891–1898.
75 X. Fu, D. Cheng, C. Wan, S. Kumari, H. Zhang, A. Zhang, H. Huyan, J. Zhou, H. Ren, S. Wang, Z. Zhao, X. Zhao, J. Chen, X. Pan, P. Sautet, Y. Huang and X. Duan, *Adv. Mater.*, 2023, **35**, 2301533.
76 Y. Li, J. Zhang, Y. Liu, Q. Qian, Z. Li, Y. Zhu and G. Zhang, *Sci. Adv.*, 2020, **6**, eabb4197.
77 J. Li, Y. Li, J. Wang, C. Zhang, H. Ma, C. Zhu, D. Fan, Z. Guo, M. Xu, Y. Wang and H. Ma, *Adv. Funct. Mater.*, 2022, **32**, 2109439.
78 M. Liu, R. Zhang, L. Zhang, D. Liu, S. Hao, G. Du, A. M. Asiri, R. Kong and X. Sun, *Inorg. Chem. Front.*, 2017, **4**, 420–423.
79 X. Peng, J. Hou, Y. Mi, J. Sun, G. Qi, Y. Qin, S. Zhang, Y. Qiu, J. Luo and X. Liu, *Nanoscale*, 2021, **13**, 4767–4773.
80 H.-Y. Sun, G.-R. Xu, F.-M. Li, Q.-L. Hong, P.-J. Jin, P. Chen and Y. Chen, *J. Energy Chem.*, 2020, **47**, 234–240.
81 Y. Jin, Y. Liu, R. Wu and J. Wang, *Chem. Commun.*, 2024, **60**, 1104–1107.
82 B. K. Boggs and G. G. Botte, *J. Power Sources*, 2009, **192**, 573–581.
83 Q. Xue, Y. Zhao, J. Zhu, Y. Ding, T. Wang, H. Sun, F. Li, P. Chen, P. Jin, S. Yin and Y. Chen, *J. Mater. Chem. A*, 2021, **9**, 8444–8451.
84 S. Hu, Y. Tan, C. Feng, H. Wu, J. Zhang and H. Mei, *J. Power Sources*, 2020, **453**, 227872.
85 M. Zhang, H. Li, X. Duan, P. Zou, G. Jeerh, B. Sun, S. Chen, J. Humphreys, M. Walker, K. Xie and S. Tao, *Adv. Sci.*, 2021, **8**, 2101299.
86 J. Wang, S. Qing, X. Tong, K. Zhang, G. Luo, J. Ding and L. Xu, *Appl. Surf. Sci.*, 2023, **640**, 158330.
87 C. Jo, S. Surendran, M.-C. Kim, T.-Y. An, Y. Lim, H. Choi, G. Janani, S. Cyril Jesudass, D. Jun Moon, J. Kim, J. Young Kim, C. Hyuck Choi, M. Kim, J. Kyu Kim and U. Sim, *Chem. Eng. J.*, 2023, **463**, 142314.
88 W. E. Du, Y. Y. Feng, J. H. Jiang, T. Zhao, G. C. Xu and L. Zhang, *J. Alloys Compd.*, 2024, **970**, 172517.
89 Y. Zheng, P. H. Tang, X. X. Xu and X. G. Sang, *J. Solid State Chem.*, 2020, **292**, 121644.
90 K. Zhang, S. Wang, X. Li, H. Li and Y. Ni, *Small*, 2023, **19**, 202300959.
91 H. Jiang, M. Sun, S. Wu, B. Huang, C. S. Lee and W. Zhang, *Adv. Funct. Mater.*, 2021, **31**, 2104951.
92 X. K. Li, X. J. Cui and L. H. Jiang, *Catal. Commun.*, 2022, **162**, 106390.
93 M. Yang, Y. M. Jiang, M. J. Qu, Y. C. Qin, Y. Wang, W. Shen, R. X. He, W. Su and M. Li, *Appl. Catal., B*, 2020, **269**, 118803.
94 X. C. Xu, H. J. Liao, L. Huang, S. J. Chen, R. Wang, S. Wu, Y. X. Wu, Z. P. Sun and H. T. Huang, *Appl. Catal., B*, 2024, **341**, 123312.
95 Z. G. Yuan, X. Sun, B. Gao, Z. G. Fan, P. X. Yang and Z. B. Feng, *Chem. Eng. J.*, 2024, **499**, 156647.
96 H. Yu, S. Zhu, Y. Hao, Y.-M. Chang, L. Li, J. Ma, H.-Y. Chen, M. Shao and S. Peng, *Adv. Funct. Mater.*, 2023, **33**, 2212811.
97 R. Deng, W. Jiang, T. Yu, J. Lu, B. Feng, P. Tsiakaras and S. Yin, *Chin. J. Struct. Chem.*, 2024, **43**, 100290.
98 X. Zhuo, W. Jiang, T. Yu, G. Qian, J. Chen, H. Yang and S. Yin, *ACS Appl. Mater. Interfaces*, 2022, **14**, 46481–46490.
99 G. Meng, Z. Chang, L. Zhu, C. Chen, Y. Chen, H. Tian, W. Luo, W. Sun, X. Cui and J. Shi, *Nano-Micro Lett.*, 2023, **15**, 212.
100 S. Zhang, C. Zhang, X. Zheng, G. Su, H. Wang and M. Huang, *Appl. Catal., B*, 2023, **324**, 122207.
101 K. Li, X. Cen, J. He and Y. Tong, *Chem. Commun.*, 2023, **59**, 5575–5578.
102 Y. Li, X. Yu, J. Gao and Y. Ma, *J. Mater. Chem. A*, 2023, **11**, 2191–2202.
103 H.-Y. Wang, S. Zhai, H. Wang, F. Yan, J.-T. Ren, L. Wang, M. Sun and Z.-Y. Yuan, *ACS Nano*, 2024, **18**, 19682–19693.
104 Y. Feng, Y. Guan, L. Wen and Y. Liu, *J. Mater. Chem. A*, 2024, **12**, 20300–20306.
105 K. Li, J. He, X. Guan, Y. Tong, Y. Ye, L. Chen and P. Chen, *Small*, 2023, **19**, 2302130.
106 K. Li, G. Zhou, Y. Tong, Y. Ye and P. Chen, *ACS Sustainable Chem. Eng.*, 2023, **11**, 14186–14196.
107 U. P. Suryawanshi, U. V. Ghorpade, P. V. Kumar, J. S. Jang, M. He, H. J. Shim, H. R. Jung, M. P. Suryawanshi and J. H. Kim, *Appl. Catal., B*, 2024, **355**, 124165.
108 Y. Zhang, D. Ma, Y. Lei, T. Zhu, J. Hu, Y. Tang, Z. Chen, J. Huang, Y. Lai and Z. Lin, *Nano Energy*, 2023, **117**, 108896.

